ATOMIC OXYGEN AND HEAT RELEASE RATE MONITORING IN HYDROGEN TUBULAR FLAMES

By

Garrett Joseph Marshall

Dissertation

Submitted to the Faculty of the

Graduate School of Vanderbilt University

in partial fulfillment of the requirements

for the degree of

DOCTOR OF PHILOSOPHY

in

Mechanical Engineering

May 14, 2021

Nashville, Tennessee

Approved:

Robert W. Pitz, PhD, PE

Haoxiang Luo, PhD

Greg D. Walker, PhD

Jason G. Valentine, PhD

Lauren E. Buchanan, PhD

ACKNOWLEDGEMENTS

*"The human heart directs the way, but the Lord plans the **steps**."* Proverbs 16:9
*"Jesus replied, "The first [commandment] is this: 'Hear, O Israel! The Lord our God is Lord alone! You shall love the Lord your God with all your heart, with all your soul, with all your **mind**, and with all your strength.'"* Mark 12:29&30
*"In all circumstances give **thanks**, for this is the will of God for you in Christ Jesus."* 1 Thessalonians 5:18

I thank God for the unanticipated experiences, the mental training, and the internal/external struggles/successes brought about by conducting this research. I pray we can wish-the-good-for (love) one another through our differences to give everyone equal opportunities to excel in their own way.

This work was supported by the National Science Foundation [Grant CBET- 1606005] and the Air Force Research Laboratory under contract No. FA8650-15-D-2518.

I want to thank Dr. Robert Pitz for 1) obtaining the above funding 2) for taking me in, and 3) for his continued support and advice throughout this research. I also want to thank my committee members, Drs. Haoxiang Luo, Greg Walker, Jason Valentine, and Lauren Buchanan for their time and effort in reviewing this work. I would like to similarly thank our collaborators from Spectral Energies/Wright-Patterson Air Force base for their efforts and reviews. Without Sukesh Roy, Hans Stauffer, Daniel Richardson, Patrick Walsh, and Stephen Grib this work could not have been carried out.

Thanks are also due to Carl Hall for his many discussions and continued support regarding the incredible code he has created and to Dr. Yinguang Ju of Princeton for his helpful conversation on tracking heat release.

My lab mates deserve a load of gratitude for their encouragement, empathy, physical and mental support, and general tolerance of me when I'm working grumpily. Thank you, Chad

Carpenter (who brought me to Vanderbilt), Darren Tinker, Marsalis Pullen, Harshini Devathi, Connor Strawn, and Conrad Reihsmann (?).

The grad school process would have been more difficult without the amazing Mechanical Engineering Department staff and my fellow grad students. Among the latter, I want to particularly acknowledge and thank Janna Rathert, Shane King, Seth Thomas, Wahid Uzzaman, Emily Matijevich, Margaret Rox, Rachel Teater, and David Ziemnicki for their camaraderie and leadership of the Mechanical Engineering Graduate (Student) Association. Thanks also extend to all of my contemporaries whose company will be greatly missed. Best of research, everyone!

None of this would have been possible without the love, rearing, and support of my family, particularly Linda & Greg Marshall, Mary & J. Glen Marshall, and Janet & Jack DeForrest. It can be difficult to understand exactly what I've been doing these past few years, but thank you for all of your encouragement. Love y'all!

Finally, someone who fits into multiple of the above categories and more, these last couple of years have been much more enjoyable with Caroline Winters. Not only has she been able to empathize and offer technical and professional advice, but she has also been a resource for thoughtful conversation, a wonderful cooking companion, an incredible adventure buddy, and surprisingly supportive and encouraging of this goofy guy. Thank you, Love!

TABLE OF CONTENTS

Page

LIST OF FIGURES

LIST OF TABLES

NOMENCLATURE

Acronyms

DNS	Direct Numerical Simulation	OPA	Optical Parametric Amplifier
EMCCD	Electron-Multiplying Charge-Coupled Device	PIV	Particle-Imaging Velocimetry
fs-TALIF	Femtosecond, Two-photon Absorption Laser-Induced Fluorescence	PM	Premixed
HRR	Heat Release Rate	SNR	Signal-to-Noise Ratio
IRO	Intensified Relay Optics	VUV	Vacuum Ultraviolet
LIF	Laser-Induced Fluorescence		

English Letters

A	Spontaneous transition rate	Q	Total quenching rate
C	LIF calibration coefficient	Q_{rad}	Radiation heat loss
c_p	Mixture specific heat at constant pressure	$\boldsymbol{q}$	Heat flux field
D_{QE}	Detector quantum efficiency	q	Heat flux
$\mathcal{D}$	Mass diffusion coefficient	R	Outer nozzle diameter (24 cm)
E	Laser energy	r	Radial coordinate
H	Pressure eigenvalue	S	Signal intensity
h	Enthalpy	$\mathcal{S}$	Set of *n* chemical species
h_p	Planck's constant	T	Temperature
I	Radial and azimuthal pressure	t	Time
I_L	Laser irradiance	U	Velocity field
K	Quenching rate coefficient	u	Radial velocity component
K	Raman calibration coefficient matrix	V	Volume
Le	Lewis number	v	Tangential velocity component
M	Detector gain	v_i	Relative velocity of species
m	Mean molar mass	W	Axial velocity gradient
N	Species number density	X	Mole fraction
N_c	Number of flame cells	Y	Mass fraction
n	Electronic transition/ number of chemical species	z	Axial coordinate

Greek Letters

α	Thermal diffusivity	σ	Quenching cross section
θ	Tangential coordinate	$\sigma^{(2)}$	Two-photon absorption cross-section
κ	Stretch rate	Φ	Equivalence ratio
μ	Mixture viscosity	χ	Thermal diffusion ratio
ν	Vibrational transition	ω	Wavelength of beam
ν_f	Frequency	ω_s	Species production rate
ρ	Density	Ω	Solid angle

Superscripts

d	Diffusion velocity
D	Dufour effect
T	Soret effect

Subscripts

0	Incident wavelength	*i*	Species number
BC	Boundary condition	*j*	Index number unless otherwise noted

CHAPTER 1

1. INTRODUCTION

In jet engines and other power generating devices, the combustion reaction/interaction is driven by turbulent mixing of fuels and oxidizers. Next generation designs require an understanding of this complex flow environment; however, it is difficult to study full-scale systems without modification. Thus, benchtop, scaled experiments are necessary to deduce the fluid physics in a fundamental and affordable manner. Once the science is understood, design iterations may be simulated for parameters such as optimal fuel consumption, peak power, and minimal detrimental emissions. Unfortunately, large, turbulent domains are computationally expensive. Reduced reaction mechanisms and flow models are thus necessary to implement the physics in a timely manner but often require a sacrifice in accuracy.

Therefore, the relevancy of these idealized models to challenging combusting environments must be determined. Laminar flames are utilized to this end for their temporally stable nature because they allow combustion characteristics to be studied with time-averaged diagnostic techniques. Additionally, the well-defined flow fields of these flames are more easily simulated. A laminar flamelet model describing lab-scale rocket exhausts was recently determined to provide necessary accuracy with minimized computation time by utilizing reduced chemical mechanisms and transport models to concisely describe local reactions [1, 2]. Extension of this methodology into a reacting, turbulent flow field, requires knowledge of local flame stretch rate (dissipation rate) and curvature to determine finite rate chemistry and understand the preferential diffusion of species [3–6]. This in turn determines the structure of the

flame, e.g. composition and temperature. Isolating the effects of stretch and curvature allows a comparison of species and temperature profiles against experimental and direct numerical simulation (DNS) results. Thus reduced and full chemical kinetic models may be validated for applicability to turbulent, combusting flows. Tubular flames represent laminar flamelets within complex combusting flows and offer control over two key flame parameters: stretch and curvature.

Interest in lean, premixed hydrogen combustion for power generation demands an understanding of heat release within these devices. When pressure fluctuations become synchronized with unsteady rates of heat release, destructive resonances can damage the combustion chamber. In this case, normalized spatial distributions of energy release are more desirable than quantitative values. Direct pressure measurements are possible through various physical and laser diagnostic techniques, but heat release must be indirectly monitored. Past evaluations have been conducted on the ability of chemical species or dilatation measurements to trace normalized heat release profiles in methane flames [7, 8]. The research demonstrated that legacy tracers were not sufficiently accurate and proposed a new method that is widely accepted today. Though less chemically complex, no such study has been carried out on hydrogen flames. Currently, OH* chemiluminescence is the only species in hydrogen flames used to trace heat release profiles; however, results of the current study suggest that this radical may not be the most accurate tracer as it is too quickly consumed in low reactivity regions [9].

1.1. Tubular Flames

Recent tubular flame studies have validated the necessity of the Soret effect (thermal diffusion) in reduced transport models [10, 11] – an effect often excluded in the past. The

researchers proposed new mixture-averaged models that could correctly account for thermal diffusion, avoiding the added complexity of multi-component models. Tubular flames have also been used to compare chemical mechanism performance in premixed methane [12] and premixed hydrogen flames [13, 14] as updated species properties and kinetics were introduced. Studies by Hall and Pitz considered major species concentrations in premixed/non-premixed hydrogen flames [11, 15] as well as concentrations of the radical species H and OH in the premixed flames [14, 16]. These types of radicals tend to be sensitive to chemical kinetic tuning within a mechanism; thus, a finer comparison between reduced mechanisms may be carried out with continued study of these and other measureable minor species.

1.2. Atomic Oxygen Radical

To avoid photolytic interference, the atomic hydrogen in Hall and Pitz's study was measured by femtosecond Two-photon Absorption Laser-Induced Fluorescence (fs-TALIF) [14, 16–18]. Atomic oxygen is another important minor species whose study is made possible by fs-TAILF and one not yet been measured in tubular flames. The concentration of atomic oxygen has implications in the simulated ignition of non-premixed turbulent flames [19] and the premixed flame that occurs at ignition in laminar mixing layers [20].

In the past, the high laser energies necessary for measurement made discerning minor species (e.g. atomic oxygen) from major species difficult. High energy deposition could dissociate oxygen-carrying species, e.g. H_2O and CO, to generate non-nascent atomic oxygen – an event known as photolytic interference. However, fs-TALIF methods have successfully measured atomic oxygen in a $CH_4/O_2/N_2$ Bunsen flame by effectively eliminating this interference [21] with high-peak-power, yet low-energy fs pulses. Signal scales with the square

of laser irradiance in this two-photon process instead of linearly meaning lower energies (≈μJ) may be used than in single-photon induced processes. The broad inherent spectral bandwidth, and short temporal durations of femtosecond pulses offer an additional advantage for driving two-photon processes in that multiple photon pairs are able to electronically excite the probed atom increasing signal (see Fig. 1 in [21]).

1.3. Heat Release Rate Monitoring

Many different radicals and properties in methane flames have been used in the past to monitor normalized heat release rates (HRR) [7]. One such property is peak dilatation rate monitored via Particle Imaging Velocimetry (PIV) [22]. The method was based on the observation that heat release directly affects gas expansion in the premixed, steady, freely propagating 1D methane flame; however, this technique fails to correlate in the presence of high stretch and curvature due to the slow response time of the expansion. Thus, dilatation rate is not expected to be appropriate for use in hydrogen flames.

Temperature is also not expected to respond quickly to heat release. Chemical reactions increase temperature within the flame zone, but the thermal energy continues to diffuse as well as convect downstream. In this case, the temperature profile would suggest heat release in areas where heat is not being generated. However, there may be some merit in considering the temperature gradient normal to the flame [23].

Paul and Najm found that the HCO radical best traced heat release within the strained methane flame [8]. Consumption of this radical occurred quickly compared to its formation rate, and its production was also directly dependent on CH_2O which, in turn, directly influenced heat release. Since HCO cannot be measured in turbulent experiments because of low fluorescence

intensity, the reaction rate was measured, instead, by a pixel-by-pixel product between normalized CH_2O and OH concentrations [8]. The rationale for this method was based on the role of CH_2O in heat production and the ability of OH to follow the initial increase in evolved heat. Both species were also involved in the production of HCO through $CH_2O + OH \rightarrow H_2O + HCO$. Other researchers have found the pixel-by-pixel technique useful for study [24–27] and some have sought to refine it [28, 29].

The above tracer method has been successful in analyzing heat release from carbon-based fuels but cannot be applied to H_2-air combustion. Thus, [OH] or it's excited state [OH*] is currently used to trace heat release rate in these flames. Clemens and Paul note the inadequacies of using the [OH] tracer insofar as it can be a misleading indicator, since it appears in low temperature regions as well as reaction zones due to slow, three-body recombination processes [30]. This effect is verified by the measurements and simulations of Hall et al. in laminar, tubular flames [11, 16]. Hall's results may also suggest that [OH*] is not a good indicator of heat release in low reactivity regions. However, little work has been done to find a better tracer in H_2-air flames since in many cases OH* zones are assumed adequate as they may appear as thin, laminar-like filaments. The current work examines alternative tracers to more accurately predict correct locations and normalized values of heat release rate.

Goodings and Hayhurst [31] give a detailed evaluation of radical recombination and equilibrated minor species in lean, H_2-air combustion. In H_2/O_2 combustion, the reactions that most sustain the flame are given by:

$$H + O_2 \rightleftharpoons O + OH \quad \text{I}$$

$$O + H_2 \rightleftharpoons H + OH \quad \text{II}$$

$$OH + H_2 \rightleftharpoons H_2O + H \quad \text{III}$$

where reaction III becomes less important in lean hydrogen flames. Instead, the following equation obtained from III – II is considered more active:

$$OH + OH \rightleftharpoons H_2O + O \qquad \text{IV}$$

The addition of $I + II + IV$ yields the overall equation $H_2 + O_2 \rightarrow H_2O + O$ for lean systems. These above reactions sustain combustion by creating a pool of radicals necessary for chain branching [31].

1.4. Document Structure

This work seeks first to present quantitative, spatially resolved atomic oxygen profiles to more fully characterize premixed, H_2/O_2 non-cellular and cellular tubular flames. A more refined approach for calibrating the fsTALIF technique to produce quantitative data is given and the reduced data is compared against three of the latest chemical mechanisms for hydrogen combustion. Secondly, heat release rate is numerically analyzed for hydrogen combustion and the adequacy of proposed tracers is discussed.

The remaining chapters are ordered as follows. First, an overview of the experimental flame and appropriate diagnostics is given followed by a chapter detailing the numerical approach for the combustion simulations. Next, three chapters relay and discuss the results of this work. The first pertains to non-cellular atomic oxygen profiles and their comparison to predictions using new chemical mechanisms, the second analyzes similar flames in a cellular configuration, and the third analyzes novel tracers for heat release monitoring in hydrogen flames. Finally, conclusions are drawn from the results of this work and succeeded by a list of references.

CHAPTER 2

2. EXPERIMENTAL OVERVIEW

2.1. Tubular Burner

Tubular flames are created when a reactive, radially-opposed flow field combusts as shown in Figure 2.1. In a premixed flame, fuel and oxidizer are mixed in an outer nozzle before exiting. Flow from the nozzle stagnates at the z-axis in the figure, and a cylindrical flame surface is formed in Figure 2.1a as the flame propagates upstream until flame speed and flow momentum are balanced. Thus, a tubular flame of a constant radius is created for a given flow configuration. This flame is one-dimensional in that all of its characteristics, i.e. temperature and chemical species profiles, may be analyzed across a radial line due to azimuthal symmetry.

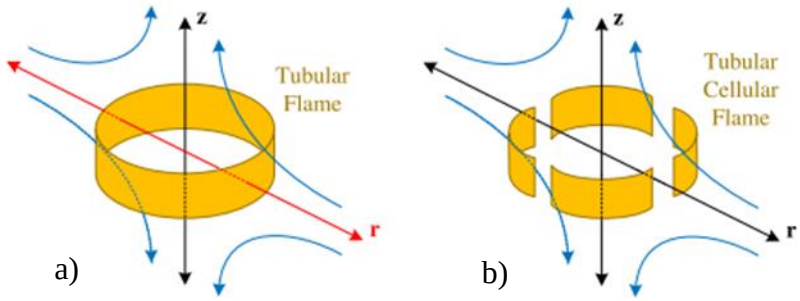

Figure 2.1. a) Non-cellular and b) cellular tubular flames.

Flame structures are affected by the non-dimensional Lewis number (*Le*) defined as the ratio of thermal diffusivity, α, to mass diffusivity, $\mathcal{D}$, or $Le = \alpha/\mathcal{D}$. For cases where $Le < 1$, mass diffuses more quickly than energy. Of the masses in the mixture, particles with smaller diameters reach the reaction zone first. This causes localized reaction enhancement compared to an equilibrium flame to produce a cellular flame structure that is broken by diminished reaction

regions as seen in Figure 2.1b. Such a configuration is azimuthally periodic and allows chemical mechanisms to be assessed across multiple flame zones (cell and dearth) at once.

Another important tubular flame parameter is flame stretch rate, κ – a factor in turbulent flames introduced by Karlovitz et al [32]. In the tubular burner, this global value is taken at the center of the nozzle, i.e. at the flow field stagnation line, in non-reacting flow and is calculated by

$$\kappa = \pi V/R \cos[\pi/2(r/R)^2] \approx \frac{\pi V}{R} \tag{2.1}$$

as derived by Wang et al. [33]. Here, V represents the radial velocity and R the outer nozzle radius. For the sub-unity Lewis number, lean premixed H_2-air flames of this study, the flame speed increases with κ leading to an increase in flame radius with κ until Damköhler effects (incomplete reaction) dominate causing the flame radius to decrease with κ until extinction [34]. Extinction normally occurs at high stretch rates where the convection time scale in the reaction zone is short compared to the reaction time (low Damköhler number [35]). In the case of lean, premixed H_2-air, tubular flame curvature enhances the flame to such a degree that higher stretch rates can be accessed than with an axially opposed burner [34].

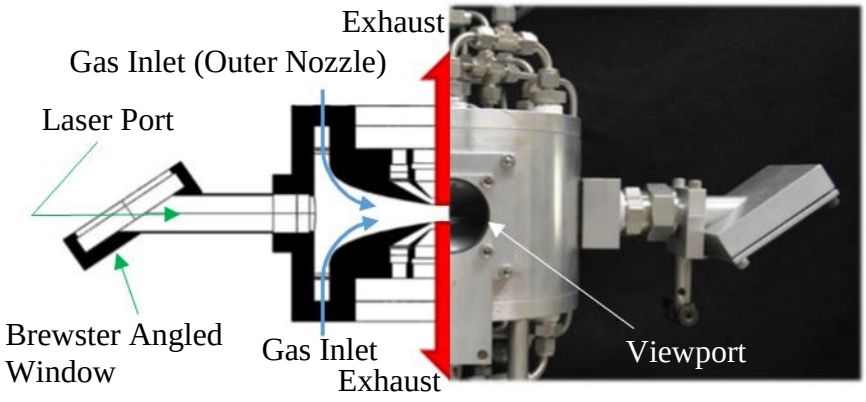

Figure 2.2. Vanderbilt's tubular burner. Left: Cutaway. Right: Equipment photo.

Vanderbilt's tubular burner (Figure 2.2) is used to study the flames. Gas enters the chamber through sintered-metal, gas inlet ports to ensure a uniform flow into the chamber while acting as a flame arrestor in the case of flash-back. It delivers the fuel-oxidizer-diluent mixture to the combusting region in premixed flames. Burnt gas exhausts through the center of the nozzle whose diameter is 24 mm with 8 mm separation between the top and bottom surfaces. Measurements may be taken at any height within this region; however, the center height (~4 mm from the top or bottom of the outer nozzle) is preferred to avoid scattering the laser light used for diagnostics when nearing the burner surface. Above and below the outer nozzle, an inert co-flow, usually N_2, is supplied in order to prevent interaction between the flame and ambient air. Figure 2.3 shows a more detailed layout of fluid flows.

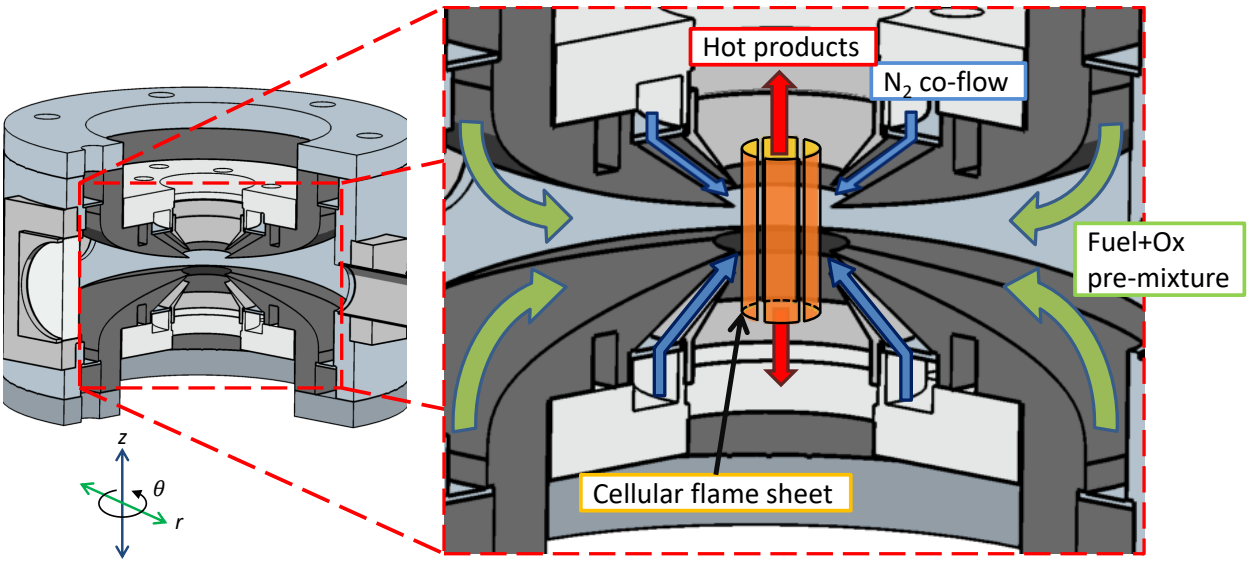

Figure 2.3. Close-up of tubular burner cutaway.

To study the flames, laser diagnostics are used since they are both non-intrusive and allow higher spatial resolution than most probe techniques. Thus, two optical ports allow a laser line to enter and exit the burner normal to the flow stagnation line as shown in Figure 2.2. The laser may be translated across the 24 mm width of the nozzle through the ports to analyze the 2D

flame domain. The Brewster angled windows allow for maximum transmissivity of the laser beam when conducting Raman scattering measurements. The ports must be positioned at least 6 cm away from the outer wall of the burner to avoid damaging the windows as the laser is focused.

This work employs premixed (PM) flames of medium to high stretch rates, about 200 s^{-1} and 400 s^{-1}, respectively. Hydrogen/oxygen flames diluted with N_2 and CO_2 provide a means to observe flames of sub-unity *Le* and to compare against various reaction mechanisms. Table 2.1 lists the flame conditions analyzed herein to determine the robustness of chemical mechanisms by varying diluent, equivalence ratio (Φ), and stretch rate (κ), on PM hydrogen. All listed species are given in terms of mole fraction. Velocity of the gases proceeding from the outer nozzle is represented by u in units of cm/s. Stretch rate, κ, is in terms of s^{-1}.

Table 2.1. Premixed hydrogen flames

O_2	N_2	CO_2	H_2	u	Le	Φ	κ
0.194	0.729		0.078	84.4	0.31	0.20	221
0.194	0.729		0.078	169.2	0.31	0.20	443
0.190	0.715		0.095	76.5	0.32	0.25	200
0.190	0.715		0.095	152.9	0.32	0.25	400
0.189		0.709	0.102	81.7	0.23	0.27	214
0.189		0.709	0.102	170.4	0.23	0.27	446
0.182		0.685	0.133	76.5	0.25	0.37	200

2.2. Laser Induced Fluorescence (LIF)

To measure minor species and atomic radicals, such as O, which do not possess vibrational modes, laser-induced fluorescence (LIF) must be employed. LIF is a two-step process in which an incident photon is absorbed and excites an atom or molecule into a higher electronic energy level as depicted by the green line in Figure 2.4. Electronic excitation occurs through

resonant interaction of the photon and species, i.e. the photon's energy must match the energy required for the electronic transition of a desired species. This makes LIF selective to a single species while producing enough signal to measure concentrations on the order of 10^{14} cm^{-3}. The excited species then relaxes to a lower energy level by emitting a photon. When the photon emitted is less energetic than the photon absorbed, the emitted wavelengths can be discriminated against any background radiation by selecting an appropriate filter. Detection limits for this diagnostic can be between 10–100 ppm in saturated LIF [36].

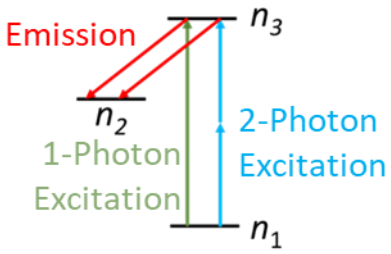

Figure 2.4. General energy diagram of LIF (green) and TALIF (blue) processes. *n* represents an electronic transition.

For atomic species, electronic excitation requires a single photon in the Vacuum UltraViolet (VUV) spectral region; this is problematic, as these photons are readily absorbed by atmospheric air before ever reaching a probe volume. Therefore, two-photons of lesser energy are utilized to excite these transitions, in a TALIF configuration, shown in blue in Figure 2.4.

An issue associated with TALIF is the erroneous generation of atomic species through laser-induced, molecular dissociation. The use of ultrafast, femtosecond pulses, mitigates this problem by delivering high intensity excitation with minimal thermal deposition, allowing TALIF measurements that are nearly photolytic-interference free [17, 37, 38]. Pulses of these time scales can still photodissociate molecules if too much energy is imparted to the flow. However, TALIF signal scales with laser irradiance squared, meaning that high signal-to-noise

ratio (SNR) may be achieved well below the point of dissociation. Additionally, femtosecond pulses are nearly transform limited, i.e. to be temporally fast, they must also be spectrally broad. This broadband pulse allows multiple frequency pairs to resonate with the electronic transition, leading to highly efficient measurements requiring less energy than traditional nanosecond TALIF.

The two-photon, LIF measurements in this work were conducted at Wright-Patterson Air Force Base (WPAFB) in Dayton, OH. An Astrella Coherent, Ti:Sapphire, fs laser produced an 800 nm beam with pulses near 85 fs at a 1 kHz repetition rate that was modified by a TOPAS-prime, collinear optical parametric amplifier (OPA) to produce tunable laser frequencies between 200-240 nm. This range allowed flexibility for the line-by-line measurements of O number densities. Burner laser windows were replaced with 3 mm thick, MgF_2 to mitigate chirp. Beam chirp through a window is a phenomenon that is most apparent in ultrafast (ps-fs) pulses. The range of light frequencies (bandwidth) in the ultrafast pulse means that a medium will induce lag on blue-shifted light. Thus, a thick window can temporally stretch the pulse width. The new window was chosen because it was both thin and had >90% transmittance in the UV. The burner was translated relative to the incoming beam and the linear measurements were compiled to map the 2D flame cross-section.

Signal was collected 90^o to the laser line through the burner's viewport. A low-pass filter of 845 nm was placed in front of the collection optics to ensure only LIF signal was captured. Signal entered a high speed, Intensified Relay Optic (IRO) to increase SNR of the minor species. An EMCCD camera was focused into the IRO to record the signal.

TALIF signal levels, *S*, are obtained by:

$$S = M\, D_{QE} \frac{\Omega}{4\pi} C\, N_i \sigma^{(2)} \frac{A}{Q + A + P + \sigma_{ion} I_L(t,\vec{r})} \iint \left(I_L(t,\vec{r})/h_p v_f \right)^2 \mathrm{d}t\mathrm{d}V \qquad (2.2)$$

where $M$and D_{QE} are the gain and quantum efficiency of detection apparatus, respectively, Ω is collection solid angle, N_i is the number density of the probed species, $\sigma^{(2)}$ is the two-photon absorption cross-section of a species [39], A is the spontaneous transition of the species, P is predissociation rate (not relevant for atomic species), σ_{ion} is the photoionization cross-section, $h_p v_f$ is photon energy, I_L is the spatial- and temporal-dependent laser irradiation, and V is the detection volume. If the $M\, D_{QE} \frac{\Omega}{4\pi} \sigma^{(2)} \iint \left(I_L(t,\vec{r})/h_p v_f \right)^2 \mathrm{d}t\mathrm{d}V$ term in Equation 2.2 remains the same between experiment and calibration, it may be omitted in the equation as it will be captured in the calibration constant, C. This is possible if collection optics, camera systems, and laser fluence are kept constant. The value of C is found by capturing signal of known species concentrations over a range of conditions similar to the experiment. Determination of this value is further discussed in Section 4.2.3. De-excitation of a measured species due to the collisional transfer of energy between the probed species and other bath gas molecules leads to reduced signal. This is accounted for by the "quenching" rate, Q. Quenching rate is determined via [36]

$$Q = N_{tot} \sum_i X_i \sigma_i v_i \qquad (2.3)$$

where N_{tot} is the total number density of the major species, X_i is the mole fraction of the i^{th} major species, σ_i is the temperature-dependent species quenching cross-section, and v_i is the relative mean speed between the measured minor species and the i^{th} major species. The two latter values are often tabulated as the volumetric quenching rate, k, where $k_i = \sigma_i v_i$ [36] and may be found in the literature [40].

The transition targeted in the experiments of this work is not significantly impacted by predissociation or ionization of O-atoms; thus these terms may be excluded from Equation 2.2. If

the optical/laser conditions between calibration and experiment remain the same, Equation 2.2 may be further reduced and rearranged to solve for atomic oxygen number density:

$$N_O = C\frac{A+Q}{A}S \tag{2.4}$$

2.3. Raman Spectroscopy

Raman spectroscopy takes advantage of an effect that occurs when incident laser light, ω_0, is inelastically scattered off of a molecule at $\omega_0 - \omega_m$, dependent on the frequency shift, ω_m, induced by the Raman cross-section of the molecule. In this technique, a laser pulse interacts with a molecule exciting it to a virtual, ro-vibrational state. Light is incoherently scattered from the molecule as it relaxes back along the red line in Figure 2.5 to a real state at a higher ro-vibrational energy level. The scattered light must be collected and focused into a spectrometer where a grating spatially separates the incoming frequencies, generating a spectrum. Each scattering species present in the measurement volume will produce a unique Raman-shifted frequency according to its atomic-bond-dependent, Raman cross-section. Raman spectroscopy is a powerful tool for identifying major molecular species; however, the inelastic scattering process is weak, and minor molecular species, whose concentrations are orders of magnitude smaller, cannot be discerned from noise.

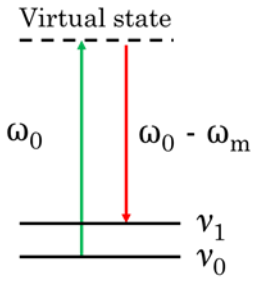

Figure 2.5. Schematic of Raman scattering process. ω represents a wavelength. ν represents a vibrational state.

To carry out Raman measurements, a Surelite Continuum III Nd:YAG (532 nm, 10 ns pulse at repetition rate of 10 Hz) was passed through a three-cavity pulse stretcher to increase pulse duration to 160 ns [41]. This allowed the ≈70 mJ of energy to be deposited by a 6 mm line with ≈180 μm beam diameter over a longer period of time to avoid laser-induced breakdown of the gas. A full domain was interrogated by translating the burner relative to the incoming beam. The beam passed through the burner's laser ports and the resulting spectra was collected 90^o to the laser line through the burner viewport. Signal entered an f/2, 3" diameter acromat and was focused onto the slit of a Spex spectrometer by a second f/7.5, 3" diameter acromat. An OG 550 filter, IR filter, optical Uniblitz shutter (6 ms opening time), an OG 550 filter, an IR filter, and a Ferroelectric Liquid Crystal (FLC) shutter (45 s opening time) created a bandpass region of 550-750 nm before the slit and reduced expose time to ~50 s. Final spatial resolution was determined to be 86 μm along the beam by a Ronchi grating. For 2D flames, the burner was translated at 200 μm increments making this the spatial resolution of the transverse domain to the beam. Calibrations were necessary to determine interference factors and signals for the major species H_2, O_2, and H_2O. A diluent of N_2 or CO_2 were also necessary to calibrate as a major species in both flames.

Raman signal was converted to absolute number densities by manipulating

$$S_i = E \sum_j K_{ij} N_j \tag{2.5}$$

where S_i is the Raman signal the i^{th} species, E is the laser pulse energy, K_{ij} is the calibration coefficient matrix, and N_j is the major species number density at the j^{th} location. Cosmic radiation and background was subtracted according to [42].

CHAPTER 3

3. DIRECT NUMERICAL SIMULATION

3.1. Non-Cellular Code

One-dimensional simulations were executed by a modified version of OPPDIF [43], a commercial code used to model axially opposed burners where reactive mixtures *flow along* an axially symmetric line while the products are *expelled* radially [13]. To produce the tubular flame, the domain is altered such that reactive mixtures *enter* radially and *exit* along the axis of symmetry to produce the tubular flame. The radial coordinate is then used as the spatial dimension through which the flame structure is mapped. The stretched flame forms in a stagnation boundary layer. Two-dimensional conservation equations are obtained from the simplification of the boundary layer assumption that relates the radial velocity to the axial velocity [44]. The resulting 1D equations are solved by finding a similarity solution to a set of reduced, non-linear, two-point boundary value problems in the radial direction [45]. A more detailed list of governing equations is provided in Appendix B.

3.2. Cellular In-House Code

The in-house tubular flame code solves the same conservation equations as OPPDIF only azimuthal symmetry is loosened to observe changes in the cross sectional structure of the flame. In other words, 2D equations are solved for radial, r, and azimuthal, θ, domains. Thus, the cellular instabilities that arise from preferential diffusion in sub unity Lewis number systems may be captured in the simulation.

3.2.1. Governing Equations

This section relates the equations found in [11]. Scalar and velocity fields are decoupled from the direction of strong axial (*z*-direction) divergence allowing the velocity field, $\boldsymbol{u}$, to be expressed in terms of a linear, axial velocity gradient, *W*, as seen below:

$$\boldsymbol{u} = u(r,\theta)\hat{\boldsymbol{r}} + v(r,\theta)\widehat{\boldsymbol{\theta}} + zW(r,\theta)\hat{\boldsymbol{z}} \tag{3.1}$$

where u and v are respectively the radial and tangential components of velocity; $\hat{\boldsymbol{r}}$, $\widehat{\boldsymbol{\theta}}$, and $\hat{\boldsymbol{z}}$ are radial, tangential, and axial unit vectors composing the basis; and r, θ, and z represent variable values for radius, azimuth, and axial coordinates within the domain.

In addition, the axial dependence of the perturbed pressure field, $\tilde{p}_1$, can be equated to a scalar pressure value, *H*, defined in Equation .

$$H = \frac{1}{z}\frac{\partial \tilde{p}_1}{\partial z} \tag{3.2}$$

The above equation is integrated allowing $\tilde{p}_1$ to be implemented as:

$$\tilde{p}_1 = \frac{z^2}{2}H + I(r,\theta) \tag{3.3}$$

where I is the radial and tangential pressure dependence.

The model consists of *n*+6 primitive variables (u, v/r, *W*, *H*, *I*, *T* [temperature], Y_i [mass fraction]) described in [11] and formulated as follows:

Mass conservation:

$$0 = \frac{\partial}{\partial r}(r\rho u) + \frac{\partial}{\partial \theta}(\rho v) + r\rho W \tag{3.4}$$

where ρ represents density.

Radial momentum conservation:

$$0 = \rho\left(u\frac{\partial u}{\partial r} + \frac{v}{r}\frac{\partial u}{\partial \theta} - \frac{v^2}{r}\right) + \frac{\partial I}{\partial r} - \frac{1}{r}\frac{\partial}{\partial r}\left(2\mu r\frac{\partial u}{\partial r}\right) - \frac{1}{r}\frac{\partial}{\partial \theta}\left[\mu\left(r\frac{\partial}{\partial r}\left(\frac{v}{r}\right) + \frac{1}{r}\frac{\partial u}{\partial \theta}\right)\right] - \mu\frac{\partial W}{\partial r} + \frac{2\mu}{r}\left(\frac{1}{r}\frac{\partial v}{\partial \theta} + \frac{u}{r}\right) \tag{3.5}$$

where μ is mixture viscosity.

Azimuthal momentum conservation:

$$0 = \rho\left(u\frac{\partial v}{\partial r} + \frac{v}{r}\frac{\partial v}{\partial \theta} - \frac{uv}{r}\right) + \frac{1}{r}\frac{\partial I}{\partial \theta} - \frac{1}{r^2}\frac{\partial}{\partial r}\left(\mu r^2\left(r\frac{\partial}{\partial r}\left(\frac{v}{r}\right) + \frac{1}{r}\frac{\partial u}{\partial \theta}\right)\right) - \frac{1}{r}\frac{\partial}{\partial \theta}\left[2\mu\left(\frac{1}{r}\frac{\partial v}{\partial \theta} + \frac{u}{r}\right)\right] - \frac{\mu}{r}\frac{\partial W}{\partial \theta} \tag{3.6}$$

Axial momentum conservation:

$$0 = \rho\left(u\frac{\partial W}{\partial r} + \frac{v}{r}\frac{\partial W}{\partial \theta} + W^2\right) + H - \frac{1}{r}\frac{\partial}{\partial r}\left(\mu r\frac{\partial W}{\partial r}\right) - \frac{1}{r}\frac{\partial}{\partial \theta}\left(\frac{\mu}{r}\frac{\partial W}{\partial \theta}\right) \tag{3.7}$$

Energy conservation:

$$0 = \rho\left(u\frac{\partial T}{\partial r} + \frac{v}{r}\frac{\partial T}{\partial \theta}\right) + \frac{1}{rc_p}\frac{\partial}{\partial r}\left(rq_r - r\sum_{i\epsilon\mathcal{S}} h_i\rho Y_i u_i^d\right) + \frac{1}{rc_p}\frac{\partial}{\partial \theta}\left(rq_\theta - r\sum_{i\epsilon\mathcal{S}} h_i\rho Y_i v_i^d\right) + \frac{1}{c_p}\sum_{i\epsilon\mathcal{S}}\left(\rho Y_i u_i^d c_{p_i}\frac{\partial T}{\partial r} + \rho Y_i v_i^d c_{p_i}\frac{1}{r}\frac{\partial T}{\partial \theta}\right) + \frac{1}{c_p}\sum_{i\epsilon\mathcal{S}}(\omega_{s_i} h_i m_i) + \frac{Q_{rad}}{c_p} \tag{3.8}$$

where c_p is specific heat capacity, q is heat flux in the radial (subscript r) or tangential (subscript θ) direction, h is enthalpy, Y is mass fraction, ω_s is species production rate, m is molar mass of a species, $\mathcal{S}$ represents the range of present species, the i subscripts represent a given species in $\mathcal{S}$, and the superscript d on the velocity terms refers to diffusive velocities.

Species conservation:

$$0 = \rho\left(u\frac{\partial Y_i}{\partial r} + \frac{v}{r}\frac{\partial Y_i}{\partial \theta}\right) + \frac{1}{r}\frac{\partial}{\partial r}\left(r\rho u_i^d Y_i\right) + \frac{1}{r}\frac{\partial}{\partial \theta}\left(\rho v_i^d Y_i\right) - \omega_{s_i} m_i, i \in \mathcal{S} \tag{3.9}$$

To enforce a uniform value for H without the velocity boundary conditions over-specifying the problem, the following is added:

$$0 = \frac{\partial H}{\partial r} \tag{3.10}$$

with the boundary condition:

$$0 = \frac{\partial H}{\partial \theta} \tag{3.11}$$

Radiation heat loss, Q_{rad}, is assumed to occur in optically-thin form for heated water and carbon dioxide as:

$$Q_{rad} = 4\sigma(T^4 - T_b^4)\, p_0 \sum_i (X_i a_i)\,, i \in \{\mathrm{H_2O}, \mathrm{CO_2}, \mathrm{CO}\} \tag{3.12}$$

where σ is the Stefan-Boltzmann constant, T_b is the background temperature, and a_i is the Planck mean absorption coefficient of species i (in [46]).

While flow acceleration is low enough to neglect pressure diffusion, mass and thermal diffusions must be considered and are expressed below in vector form:

$$\rho Y_i \boldsymbol{u}_i^d = -\sum_{j\epsilon\mathcal{S}} Y_i \mathcal{D}_{ij} \nabla X_j - Y_i \mathcal{D}_i^T \nabla \ln T\,, i \in \mathcal{S} \tag{3.13a}$$

$$\boldsymbol{q} = \sum_{i\epsilon\mathcal{S}} h_i \rho Y_i \boldsymbol{u}_i^d - \lambda \nabla T + \boldsymbol{q}^D \tag{3.14b}$$

where X is mole fraction, λ is heat conductivity, and $\boldsymbol{q}$ is the heat flux field. Thermodynamic and kinetic information in the above equations are evaluated with CHEMKIN-II [47] and the employed mechanisms are referenced within this document where appropriate. Mass diffusion coefficients, $\mathcal{D}_{ij}$, and thermal diffusion terms, $\mathcal{D}_i^T$ and $\boldsymbol{q}^D$ from the Soret and Durfour effects

respectively, are calculated with EGLIB [48] and expressed in terms of the computational variables $\widetilde{\mathcal{D}}_{ij}$ and $\tilde{\chi}_i$:

$$Y_i \mathcal{D}_{ij} = \rho \widetilde{\mathcal{D}}_{ij}, j \in \mathcal{S} \tag{3.15a}$$

$$Y_i \mathcal{D}_i^T = \rho \sum_{j \in \mathcal{S}} \widetilde{\mathcal{D}}_{ij} \tilde{\chi}_j X_j \,, j \in \mathcal{S} \tag{3.16b}$$

$$\boldsymbol{q}^D = p_0 \sum_{i \in \mathcal{S}} \frac{m}{m_i} \tilde{\chi}_i Y_i \boldsymbol{u}_i^d \tag{3.17c}$$

where the m term refers to mean molar mass when not modified by a subscript.

3.2.2. Boundary Conditions

An angular section ($r \in [0, R], \theta \in [0, 2\pi/N_c]$) of the 2D domain can be selected to force N_c-fold, flame-cell symmetry. All variables have azimuthal symmetry except for v which is set to 0 at $\theta = 0$ to prevent arbitrary rotation of the flame to arrive at the time-steady solution.

Radial boundary conditions at the outer nozzle ($r = R$) are specified by:

$$u = u_{BC}, \qquad \frac{v}{r} = 0, \qquad W = W_{BC}, \qquad Y_i\left(u + u_i^d\right) = (Y_i u)_{BC}, \qquad T = T_{BC}$$

with the following exit ($r = 0$) conditions at the centerline:

$$u = 0, \qquad \frac{v}{r} = 0, \qquad \frac{\partial W}{\partial r} = 0, \qquad \frac{\partial Y_i}{\partial r} = 0, \qquad \frac{\partial T}{\partial r} = 0, \qquad I = 0$$

3.2.3. Numerical Method

All derivatives are discretized with second-order central differencing except for the radial convective terms which are processed using first-order upwind differencing since convection is occurring in a single direction and is not significantly affected by neighboring flow vectors. Conservation equations are solved using pseudo-transient continuation in which all variables

except density are time-stepped. PETSc [49] is used to solve the system of equations. The domain is discretized with adaptive mesh refinement for a non-uniform grid in the radial direction with higher resolution around the flame front while azimuthal grid spacing is kept constant. Solution 2-norm error (aka, L2-norm, ℓ^2) is set to a tolerance of E-4.

CHAPTER 4

4. ATOMIC OXYGEN PROFILES IN NON-CELLULAR, TUBULAR FLAMES

This chapter is adapted from "Quantitative oxygen atom measurements in lean, premixed, H_2 tubular flames" published in the *Proceedings of the Combustion Institute* and has been reproduced with the permission of the publisher and my co-authors Patrick S. Walsh and Robert W. Pitz [50].

4.1. Introduction

This study measures the atomic oxygen concentration profiles in lean, premixed, 1D H_2/O_2 tubular flames diluted with N_2 and CO_2 via fs-TALIF using quench-corrected data from Raman experiments. Low- and high-stretch rate conditions are imposed on each configuration, and the measured species profiles are compared against simulations. The O-atom profiles complement profiles of other minor species, major species, and temperature already measured in the same flames [14]. The experimentally determined O-atom data is used to gauge the effectiveness of the Burke mechanism with Li carbon pathways (referred to herein as Burke-Li) [51, 52] and the newer Kéromnès [53] and Varga [54] mechanisms in determining this radical species' concentrations and profiles across flame conditions. Burke-Li contains 33 reactions and 12 species; Kéromnès contains 31 reactions and 14 species; and Varga contains the same reactions and species as Kéromnès with optimization of selected chemical kinetics.

Nitrogen is a natural diluent selection since it is the dominant species in air. Combustion with CO_2 dilution is of interest in syngas fuels derived from biomass [53, 54] and oxy-fuel combustion [55]. At flame temperatures, CO_2 becomes chemically reactive [55]. Flame speed is primarily reduced by the direct participation of CO_2 in $\mathrm{CO} + \mathrm{OH} \rightleftharpoons \mathrm{CO_2} + \mathrm{H}$ which competes

against the dominant chain-branching reaction $H + O_2 \rightleftharpoons O + OH$ for H radicals [56]. Because of this competition, CO_2 is expected to reduce the concentration of O-atoms in the tubular flames while affecting the flame temperature, flame speed, and extinction [34].

4.2. Experimental Details

The four non-cellular flames investigated in the tubular burner (Figure 2.2) and are outlined in Table 4.1**.** These conditions were previously measured with Raman scattering for major species concentrations and temperature [14]. For a stable CO_2 diluent tubular flame at the low- and high-stretch rates, the stoichiometry of the CO_2 flame needed to be higher than the N_2-diluted flame. Adiabatic flame temperatures are also given in the tables below for the reactants. Due to preferential diffusion, the actual flame temperatures of the tubular flames are measured to be ≈1300 K for non-cellular and 1600 K cellular N_2 diluted flames or ≈1400 K for non-cellular and cellular the CO_2 diluted flames [14]. Fuel-oxidizer-diluent mixture was fed into the chamber through the porous, annular inlets of the tubular burner. An N_2 co-flow was fed near the center of the burner to shield the flame from environmental debris and to provide additional nozzle cooling. Two, 50 mm Ø MgF_2 windows allowed the laser to enter and exit the chamber.

Table 4.1. 1D flame cases from Table 2.1. Species quantities are given in mole fraction.

O_2	N_2	CO_2	H_2	u (cm/s)	Le	Φ	κ (s^{-1})	T_{AD} (K)
0.194	0.729		0.078	84.4	0.31	0.20	221	925
0.194	0.729		0.078	169.2	0.31	0.20	443	925
0.189		0.709	0.102	81.7	0.23	0.27	214	890
0.189		0.709	0.102	170.4	0.23	0.27	446	890

Atomic oxygen was detected by exciting the O-atoms from $2p\ ^3P \rightarrow 3p\ ^3P$ (225.6 nm) and capturing the 844.6 nm band of light emitted in $3s\ ^3S \leftarrow 3p\ ^3P$ [57]. The 800 nm output form an Astrella Coherent, Ti:Sapphire laser was converted by a TOPAS-prime OPA to produce 85 fs pulses of 225.7 nm light (~11 nm linewidth) at 1 kHz that were focused to ~350 μm over 6 mm in the flame.

To ensure that O-atoms were not being photolytically produced in the flames, laser energy was varied from about 2–8 μJ in a Hencken burner flame with corresponding laser irradiance of 75–300 GW/cm^2. Because there was no significant alteration to the normalized signal profiles, the laser energy range was considered acceptable. The laser energy was kept near 4.4 μJ during all experiments, and the corresponding laser irradiance of 165 GW/cm^2 produced strong O-atom TALIF signals.

O-atom line measurements were captured perpendicular to the laser line through the burner's 50 mm Ø, UV fused silica viewport. Images were acquired with an IRO and EMCCD pairing. A LaVision High Speed IRO was set to an intensifier gain of 65 % with a gate width of 100 ns. The IRO collected fluorescence signal from the laser irradiation while fit with an 85 mm, f/1.8 lens and 48 mm lens tube. An 800 nm longpass filter was placed in front of the IRO to discriminate the O-atom fluorescence. The focal plane of an Andor Newton 970 Electron Multiplying, Charge-Coupled Device (EMCCD) was positioned to capture images from the IRO. A single image of the flame was integrated over 1 s (1000 laser pulses). Ten images were captured and then averaged for each flame without electromagnetic gain (10,000 total pulses).

4.2.1. Instrument function deconvolution

Signal deconvolution of the IRO/EMCCD spatial response was corrected to better compare the data and simulations [14]. The IRO/EMCCD spatial response was found to be well-modeled by a Gaussian profile with a full-width-half-max of 350 μm (spatial resolution) as estimated from imaging a knife edge. Instrument spatial response was then removed from the data by applying the *Lucy-Richardson* deconvolution algorithm within the MATLAB 2018a software package. Deconvolving the data is shown to lead to a 15% increase in maximum number density as seen in the normalized profiles of Figure 4.1.

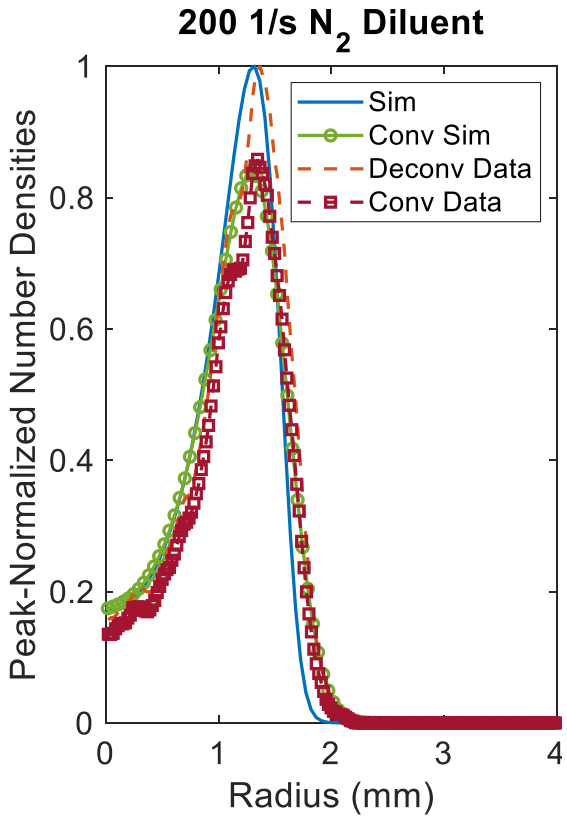

Figure 4.1. Comparison of number density profiles with and without instrument deconvolution to simulation normalized to deconvoluted maximums.

4.2.2. Quenching Considerations

Fluorescence signal was related to number density through Equation 2.2. Quenching occurs in LIF from the transfer of energy between the excited-state particle and other nascent particles. Instead of fluorescing, the probed particle loses energy by collisional interaction leading to a signal decrease determined by the fluorescence yield, $A/A+Q$. Signal can be reduced up to 300x depending on Φ as shown in Figure 4.2. The figure also shows ~50% increase in fluorescence yield when temperature-dependent quenching of H_2O is considered near the equivalence ratio of interest ($\Phi \approx 0.4$). If major species concentrations [14], quenching cross-sections, and mean speeds relative to the probed species are known, Q may be estimated through Equation 2.3 [36] in Section 2.2.

.

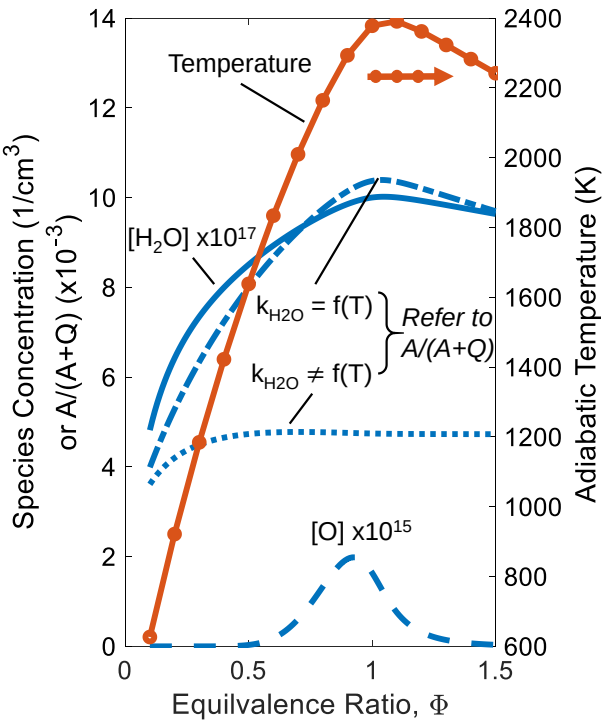

Figure 4.2. Simulated equilibrium conditions against equivalence ratio in the Hencken flame.

The equation may be simplified by introducing the quenching rate values $k_i = \sigma_i v_i$ in terms of cm^3/s [40]. While most quenchers exhibit some form of temperature dependence, temperature has been found to have a stronger effect on k_{H_2O} in atomic hydrogen quenching [14, 58]. Similarly, water quenching of atomic oxygen has been found to decrease slightly with temperature in the form of $k_{H2O} \propto T^{-0.5}$ [59, 60]. In other words, less signal dampening due to collisions with H_2O is expected to occur at higher temperatures. In this study, "no quench corrected" method will be compared to two methods O-atom quenching: one with and one without k_{H_2O} temperature dependence. These three methods are further discussed below in Calibration Methods.

4.2.3. Calibration Methods

The calibration factor, C, was determined from captured O-atom signal within a 12.5 mm diameter Hencken burner flame. Measurements were taken 20 mm downstream of the burner exit where the flame is considered to be in equilibrium for H_2-air combustion [61]. The Hencken burner was positioned under the tubular burner in such a way that the optical conditions remained the same between calibration and tubular flame experiments. O-atom fluorescence signal was monitored as mixture equivalence ratio varied from 0.6 to 1.2. Calibration (and, subsequently, tubular flame data reduction) was carried out by three methods. Method 1: No quenching correction for major species was considered, i.e., $(A + Q)/A$ was not used to determine N_O. Method 2: Temperature-independent quenching of major species was considered (constant k value of quencher with temperature). Method 3: Temperature-dependent quenching from H_2O was considered proportional to $T^{-0.5}$ (discussed in the previous section). A chemical

equilibrium solver in Cantera [62] was used to calculate equilibrium O-atom number densities as well as equilibrium major species concentrations in the Hencken flame to determine quenching rates for calibrating Methods 2 & 3.

Figure 4.3 (left axis) maps calculated O-atom number densities to measured signal for Method 1. Values on the right axis correspond to Methods 2 & 3 where quenching correction has been considered. By plotting $N_O\ A/(A+Q)$ in Methods 2 & 3, the calibration factor becomes independent of the calibration bath gas and may thus be applied to any experimental flame under the same optical, laser, and acquisition conditions. Method 1, therefore, is not expected to yield accurate results when applied to an environment whose bath gas differs from the calibration. The slope of the best-fit lines in Figure 4.3 determined the values of C.

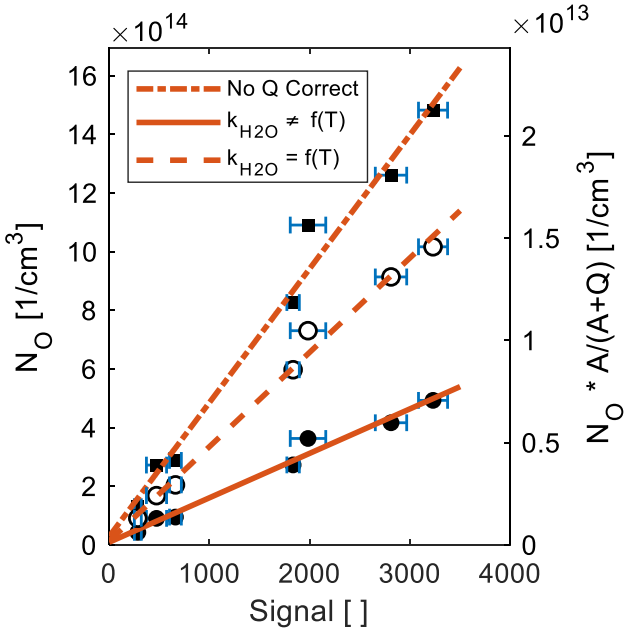

Figure 4.3. Resulting calibration curves from H_2-air Hencken burner measurement. Left axis: No quenching correction. Right axis: Temperature-independent and -dependent quenching of water considered.

Figure 4.4 shows the experimental and calculated O-atom concentrations with varying equivalence ratio in a Hencken flame. Data was reduced using Equation 2.4. All of the proposed methods agree well with calculated equilibrium number densities, but Method 3 gives a better fit to the leanest condition ($\Phi = 0.6$).

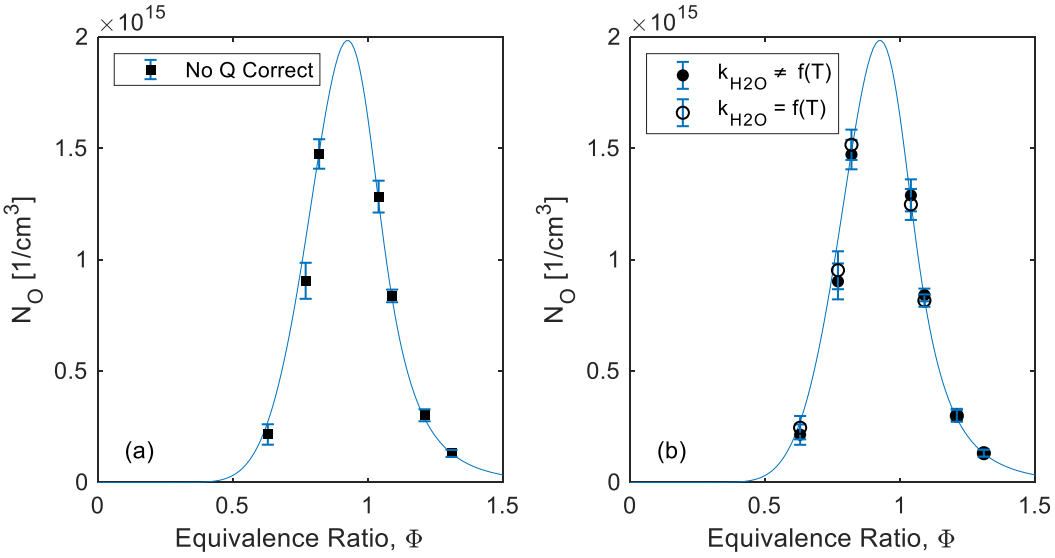

Figure 4.4. Experimental O-atom number densities determined in H_2-air Hencken flame. The solid line represents equilibrium concentrations calculated with Cantera [62].

4.3. Results & Discussion

Shown in Figure 4.5 are the simulated O-atom profiles across the radii of the flames along with the O-atom profiles from fs-TALIF measurements as determined from the three data reduction methods. Uncertainty bands have only been placed at the peak number density values with slight offsets for clarity. Uncertainty bands have been omitted from Method 1 (no quenching correction). The only quantifiable uncertainty in this method is the shot-to-shot signal noise which was imperceptible in the reduced data due to the 10,000 pulse average. For the other methods, error bars were calculated using the standard deviation of the fs-TALIF signal in

conjunction with uncertainties incurred from the k values of quenching species [40] and Raman measurements (mole fractions $\pm$2%, temperatures $\pm$50K) [14]. Uncertainty calculations are further discussed in Appendix A. The distributions behave as expected with a sharp increase near the flame front that quickly fades as the radical is consumed. Number densities also increase with stretch rate as anticipated for both cases of diluent.

As mentioned, the positive flame front curvature enhances combustion through preferential diffusion. This can lead to 80% higher, local mixture fractions within the flame [11]. Thus, higher-than-adiabatic atomic oxygen concentrations are achieved. A comparison between Figure 4.4 and the simulation/data of Figure 4.5 demonstrates that atomic oxygen concentrations in the tubular flames are super-equilibrium. For an equilibrated flame of $\Phi = 0.2$, O-atom signal cannot be detected. Increasing Φ of the adiabatic flame by 100% to Φ = 0.4, corresponding to expected Φ increase from preferential diffusion, yields a number density of around 2.5 x 10^{12} 1/cm^3 which is still over 1000x less than what is seen in the tubular flame.

Little difference is found between the mean values of Method 1 (no quenching) and Method 2 [$k_{H2O} \neq f(T)$] calibrations in the N_2 diluted hydrogen flames of Figure 4.5. This is because the number density of H_2O in the reacting region of the tubular flame is on the same order of magnitude as those in the calibration flame. In addition, temperature dependent quenching effects are ignored leading to similar mean values. Hydrogen molecule and O_2 concentrations are higher within this region of the tubular flame, but the increase does not significantly influence overall quenching.

A more substantial difference between Methods 1 and 2 is apparent in the CO_2 diluted tubular flame as water number densities differ between the calibration and experimental flame. Diluent quenching also contributes to the discrepancy here since it is present in large quantities

and $k_{CO_2} > k_{N_2}$. Therefore, it is essential to include quenching effects when composition differences exist between the calibration and studied flames.

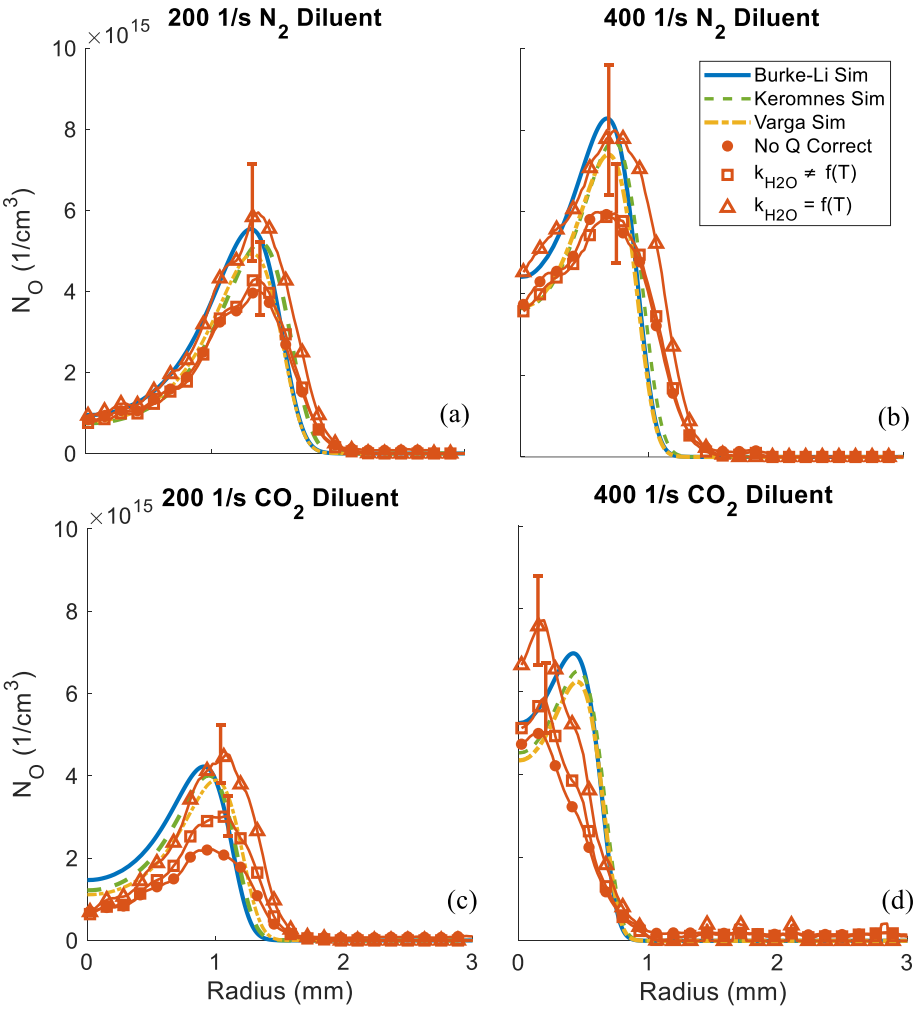

Figure 4.5. Atomic oxygen data profiles (symbols) versus radial coordinate. The simulated profiles (lines) use a 50 s^{-1} stretch rate boundary condition, *W*, at the nozzle exit.

The value of k_{H_2O} has been chosen to vary with temperature by $T^{-0.5}$ because of its significantly larger value compared to other present quenchers. As shown in Figure 4.5, flames diluted with N_2 in (a) and (b) agree relatively well with the mean of the temperature-dependent quenching corrected data. This is not so for the CO_2 diluted flame of (c); however, peak number

densities of the simulations still lie within the error bars of the data with k_{H_2O} temperature dependence. The inlet boundary condition for stretch rate is not yet well characterized in the tubular burner; thus, a slight radial shift occurs between the data and simulation of Figure 4.5c.

One may notice Hall and Pitz [14] found that simulations better matched temperature-independent quenching of H-atoms in CO_2 diluted flames. The previous study did not change the value C between the two methods (no T-dependence and T-dependence of k_{H_2O}). Figure 4.3 shows that the calibration slope of the non-temperature-dependent curve, and thus the value of C, can be up to half the value of the other. If this reduced value is applied to Fig. 4 of the previous paper [14], simulated profiles approach data profiles with T-dependent quenching.

Along with the data, Figure 4.5 contains simulated atomic oxygen concentration predictions based on the chemical kinetics of Kéromnès [53], Varga [54], and the Burke-Li mechanism [51, 52] which has yielded good agreement between past tubular flame simulation and data [14]. Peak number density values for all mechanisms fall within the uncertainty of the T-dependent quenching corrected data.

Profile shapes between the simulations and data vary slightly in all cases. The low-stretch, N_2 diluted flame data (Figure 4.5a) show very strong agreement with the Kéromnès mechanism with little spatial variation. One will notice a kink in the O-atom profile on the product side of the data. This is believed to be a result of the uncertainty in the data rather than of increased atomic oxygen production. The high-stretch, N_2 diluted flame of Figure 4.5b also shows reasonable agreement between data and simulations though O-atom production is predicted to occur slightly after the data suggests. This may be due to slight fluctuations in the circularity of the flame while being averaged at the high-stretch rate thus widening the profile. Concentrations near r = 0 mm are well determined by the mechanisms.

Flames diluted with CO_2 are shown to have higher spatial discrepancy between atomic oxygen concentration data and simulation than those diluted with N_2. In the 200 s^{-1} stretch case (Figure 4.5c), the simulated peak has a radius ~0.2 mm less than the measured. The 400 s^{-1} flame (Figure 4.5d), however, predicts a larger radius than measured with peak O-atom concentration matching the Burke-Li value. This profile shift cannot be accommodated by the 30–60 s^{-1} stretch-rate-at-the-boundary (*W*) range. Data from the low-stretch case is believed to be accurate suggesting that transport parameters for high temperature atomic oxygen in the presence of carbon dioxide must continue to be improved.

For the high-stretch flame, discrepancy is partly due to uncertain flow conditions. The CO_2 flow became unsteady after long periods of use due to pressure regulator freezing. This also means that gas flow temperature into the burner could be lower than expected. If so, lower boundary temperatures would weaken the flame speed causing a decreased flame radius as observed. Poor temperature control also means inaccurate flow rates as the product of the specific heat capacity and density of CO_2 increase by 5 % from 273 K (used for gas properties in flow meter calibration) to 293 K. Simulations over the possible, higher flow rates (*ergo* higher global stretch) continue to predict number densities within the uncertainty bands but without much change in radial location of the peak. While flames with stretch rates (κ) of 500 s^{-1} are numerically calculable, experimentally the stretch rate cannot be increased above the current conditions without extinguishing the flame. Thus, it is possible that flame profiles may be difficult to predict near extinction.

Since all chemical mechanisms perform comparably for this O-atom minor species, they are expected to show similar results in other H_2/O_2/diluent flames. The added kinetics for syngas

in the Kéromnès and Varga mechanisms do not appear to offer substantial advantage over the Burke-Li mechanism with kinetics for CO, CH_2O, and CH_3OH combustion from Li.

4.4. Conclusions

Quantitative O-atom measurements in high- and low-stretch rate tubular flames diluted with N_2 and CO_2 have been presented using fs-TPLIF signal quench corrected from Raman measurements. Quenching effects are imperative to consider when the composition and temperature of the calibration and experimental flames differ. Simulated profiles showed best agreement in all cases when temperature-dependent quenching of H_2O was considered in the data. This agrees with H-atom simulations which suggest temperature-dependent quenching must be considered when the calibration factor is adjusted per method used in Fig. 4 of [14]. All tested chemical mechanisms predicted O-atom profiles within the uncertainty of the data and comparably predicted the profile geometries, but the Burke-Li mechanism appears to better capture the mean of the data.

CHAPTER 5

5. ATOMIC OXYGEN PROFILES IN CELLULAR TUBULAR FLAMES

5.1. Experimental Details

The three cellular flames investigated in the tubular burner (Figure 2.2) and are outlined in Table 5.1. These conditions were previously measured with Raman scattering for major species concentrations and temperature [63]. The O-atom profiles complement profiles of other minor species, major species, and temperature already measured in the same flames [16, 42, 63]. Adiabatic flame temperatures are also given in the tables below for the reactants. Due to preferential diffusion, the actual flame temperatures of the cellular tubular flames are measured to be ≈1600 K for N_2 diluted flames or ≈1400 K for the CO_2 diluted flames [16, 42, 63].

Table 5.1. 2D flame cases from Table 2.1. Species quantities are given in mole fraction.

O_2	N_2	CO_2	H_2	u (cm/s)	Le	Φ	κ (s^{-1})	T_{AD} (K)
0.190	0.715		0.095	76.5	0.32	0.25	200	1060
0.190	0.715		0.095	152.9	0.32	0.25	400	1060
0.182		0.685	0.133	76.5	0.25	0.37	200	1068

These flames were studied and their data reduced in the same manner as the non-cellular (see Section 4.2) with minor modifications. The 2D nature of the cellular flames required a scan of the domain. Thus, the tubular burner was initially translated in 0.5 mm steps relative to the beam. After measuring the Φ=0.25, 200 s^{-1} flame, this value was determined to be too high (discussed below), and the remaining flames were measured at 0.25 mm steps.

At low stretch rates, rotation of the flames was prevented by adjusting the mass flow rate of the co-flow. This stabilization method was not possible in the high-stretch case, so a thin wire was introduced near a flame cell. The flame was then anchored at the cost of inducing asymmetry in the corralled cell. Measurements on this flame were thus performed on the cell diametrically opposed to the wire location.

Finally, data for this campaign was quench corrected using temperature dependence on the volumetric quenching rate of H_2O. This method more fully accounted for actual physical conditions and accurate legacy simulations agreed with the data reduced in this way [50].

5.1.1. Mapping Two-Dimensional, Cellular Flame Data

After deconvoluting the data, the resulting signal lines from each translated step of the burner were stacked together as shown in Figures 5.1 and 5.2. The images show that the laser was able to capture signal across the diameter of the flame. Another readily apparent feature is the resolution between the two figures. The low stretch, nitrogen diluted flame of Figure 5.1 was compiled by translating the burner at a step size of 0.5 mm. This value was selected because it was near the approximate focused beam diameter (350 μm) and allowed for timely data capture. However, the resolution of the cells in the piecewise reconstruction suggested that this value was not sufficient, and the remaining flames were captured by translating the burner in 0.25 mm increments as shown in Figure 5.2.

To better compare the 2D reconstructions to simulations, linear interpolation was applied to the data using MATLAB's native "interp2" function. As intuited and seen in Figures 5.1 and 5.2, the resulting profiles were dependent upon the initial burner step size.

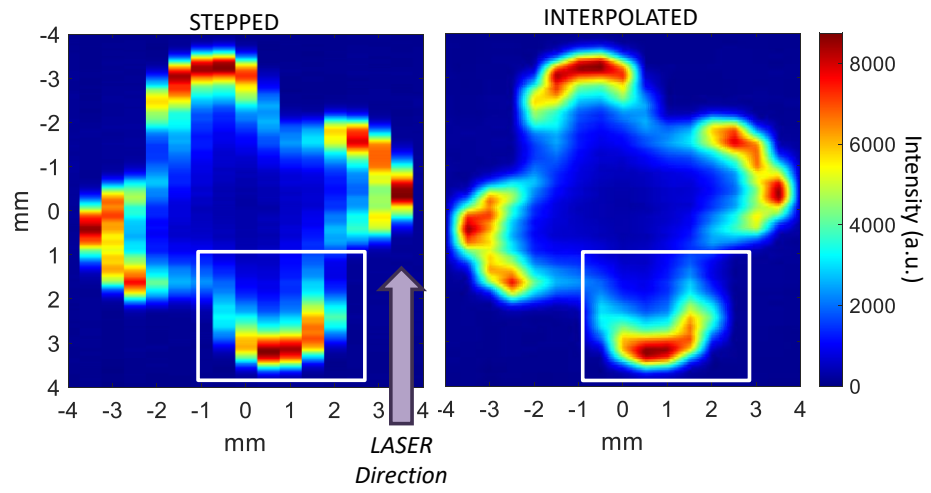

Figure 5.1. Raw data reconstruction of N_2-diluted flame stepped at 0.5 mm. The cell in the white rectangle is analyzed below.

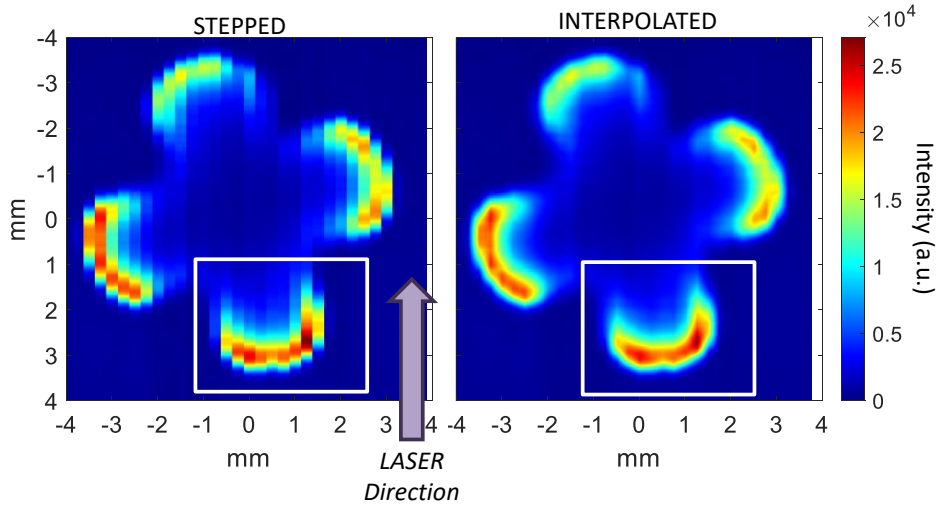

Figure 5.2. Raw data reconstruction of CO_2-diluted flame stepped at 0.25 mm. The cell in the white rectangle was analyzed below.

5.2. Results and Discussion

5.2.1. N_2-diluted flame

Figure 5.3 compares simulated 2D O-atom profiles using the three chemical mechanisms against fs-TALIF measurements. The data shown has been linearly interpolated to smooth its

profile facilitating comparison with simulations. A curved cell with regions of reduced reactivity on either side is clearly visible in the data. The asymmetry of the measured cell is a result of the low resolution of the scan of Figure 5.3(a) where the laser line was only translated 0.5 mm at a time (cf. Figure 5.1). Slight rotations of the flame may also have occurred after translating the burner leading to the small amount of asymmetry in Figure 5.3(b). Cell thickness appears comparable between the measurements and simulations in each flame case; however, their arc lengths are noticeably different in the 200 s^{-1}, N_2-diluted flame. Regarding the comparatively reduced cell length of the data, this may again be a result of the 0.5 mm step, but there is also variation in length between the simulated profiles. The BurkeLi mechanism produces a cell with O-atoms evenly distributed from its center to its edges as anticipated at the given conditions. Cells produced from the remaining mechanisms appear to have thicker regions of high O-atom concentrated near the edges. This could be due to the slightly higher flame speed predicted by Kéromnès and Varga compared to BurkeLi.

The increased flame speed of Kéromnès in Figure 5.3(a) results in a longer and flatter cell compared to the others. (Another effect of flame speed may be seen in Figure 5.4(a) and Figure 5.4(b) where the cell and dearth profiles are shifted). This may likely have been caused in part by the researchers' reevaluation of species' thermodynamic properties. Additionally, both the Kéromnès and Varga mechanisms have slightly modified pre-exponential factors, *A*, and reaction efficiency factors, ϵ, for the $H + O_2 + M = HO_2 + M$ reaction. According to the sensitivity analysis of Burke *et al*., flame speed was most affected by this reaction for their flame at 10 atm [51]. Modifying these features of the BurkeLi mechanism with *A* and ϵ from Kéromnès, however, does not change the predicted profiles of BurkeLi. Reactions within a mechanism are

intimately interdependent; thus, the very slight difference in flame speed shown is, instead, the result of a number of interactions.

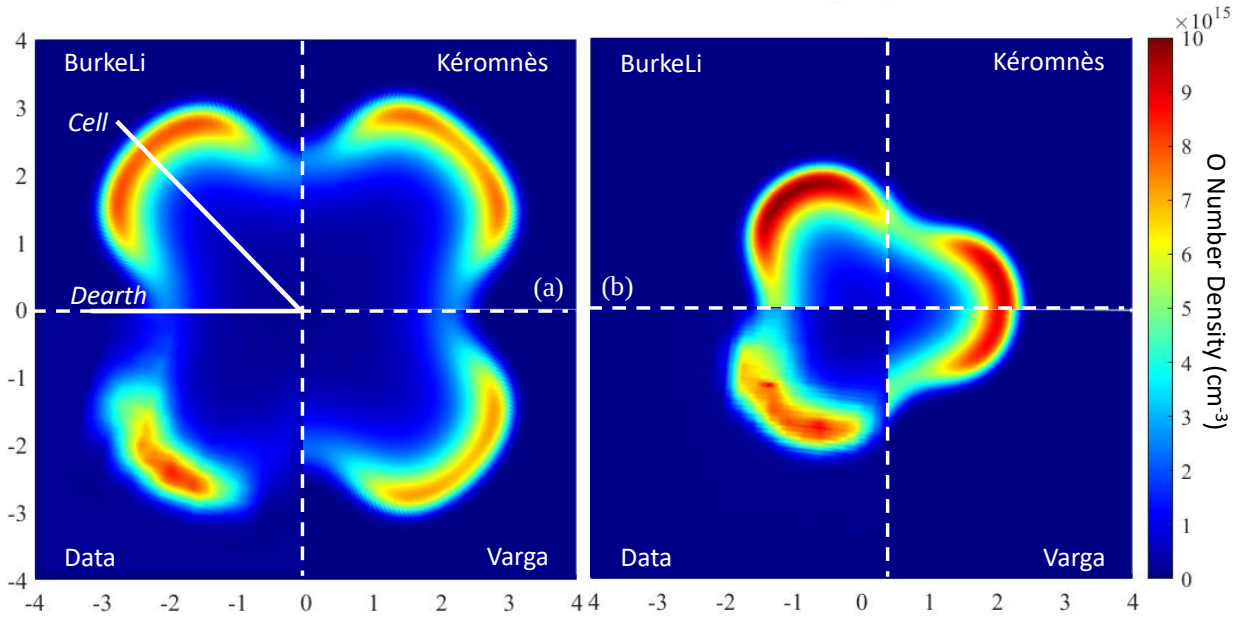

Figure 5.3. Comparison of 2-D profiles between simulations employing various chemical mechanisms and O-atom data for N_2-diluted tubular flames at κ=200 s^{-1} (a) and κ=400 s^{-1} (b). Stretch rate boundary conditions for 4- and 3-cell flames were 50 s^{-1} and 130 s^{-1}, respectively. Highlighted lines in (a) indicate the 1D radial profile locations for the cell and dearth regions of Figures 5.4 and 5.9.

One-dimensional plots like the one in Figure 5.4 show atomic oxygen concentrations through the cellular and dearth regions (as noted in Figure 5.3(a)) of the measured flames for both data and simulations produced from various mechanisms. Error bars are shown at the peak locations of the profiles in the cell and dearth regions. The non-zero stretch rate boundary conditions, *W*, at the nozzle exit (noted in Figure 5.3 and later Figure 5.8) were selected based on past work by Hall [42]. Stretch rate at the exit of the nozzle (r=12 mm) should not be confused with κ which represents the global stretch rate.

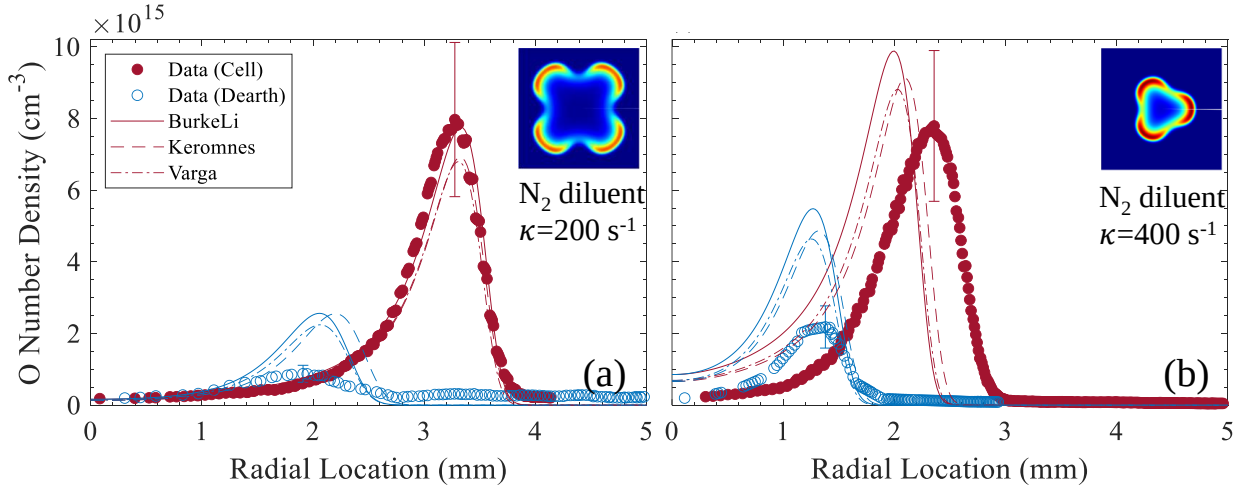

Figure 5.4. Cell and dearth O-atom profiles extracted from Figure 5.3.

Examining the low-stretch, N_2-diluted flame in the 1D plot of Figure 5.4(a), the BurkeLi mechanism predicts the mean value of the O-atom data through the cell very well. The remaining mechanisms still predict concentrations in the cell within the uncertainty of the data while capturing the radial location of the cell. The mean, peak concentrations in the dearth region is, however, not captured by any mechanism.

Other minor species have also been comparably predicted at this flame condition. As an example, atomic hydrogen profiles have been extracted from the data of [16] and supplied here in Figure 5.5. Figure 5.5(a) shows a good agreement between data and simulation of peak H-atom number densities. However, the simulation does not capture the width of the data profiles very well, and more H-atom is found in the product zone than predicted.

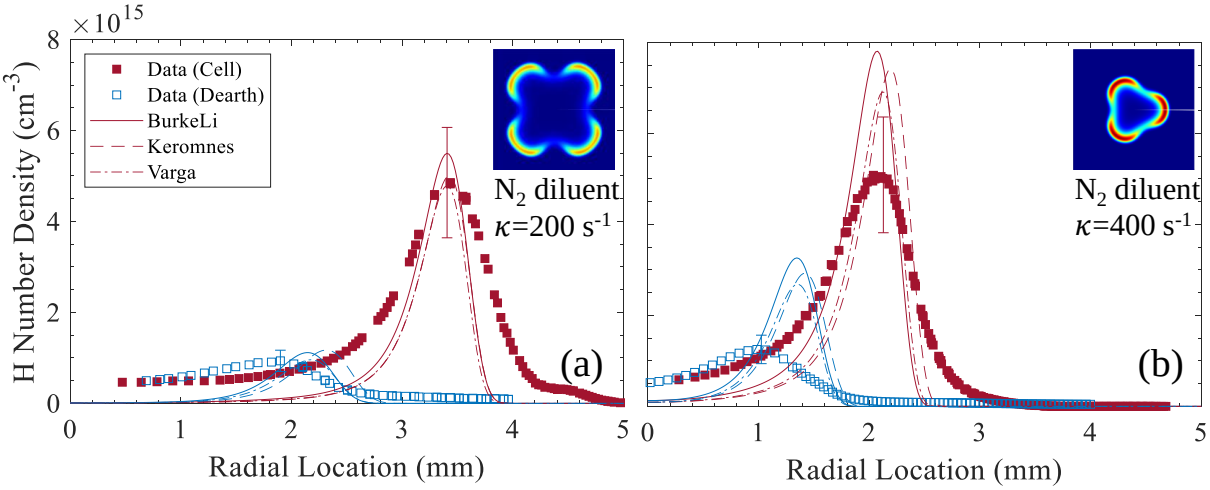

Figure 5.5 Cell and dearth H-atom profiles extracted from Figs. 3 and 4 of [16].

The atomic oxygen, 1D data profile for the cellular region of Figure 5.4(b) appears the same as Figure 5.4(a) despite doubling the stretch rate. This is consistent with previous findings in H and OH measurements of cellular flames [16]. Figures 5.4 and 5.5 show the cells simply shifting radially inward as stretch-rate increases without affecting minor species number densities. Such a trend differs from 1D non-cellular flames whose minor species concentrations were found to increase with stretch rate [14, 50]. In 1D non-cellular, lean H_2-air tubular flames, the number densities of species such as H, O, and OH increase as stretch rate increases due to preferential diffusion as the flame radius is reduced [14, 50]. No such increase is seen in the 2D cellular data since the cells move inward without any substantial change in their curvature (constant at ≈1/mm from [63]) or flame thickness (≈0.7 mm full-width at half-maximum from Fig. 5).

A change in curvature would indicate a change in flame structure. Temperature and minor species profiles in particular are sensitive to the corrected Karlovitz number that includes the product of the flame thickness and curvature (discussed in [34]). The data of Figures 5.3 and 5.4 show cells of similar curvature and thickness contributing to the expectation of similar

number densities. Likewise, the maximum temperature of the flames appears unaffected by stretch rate as shown in Figure 5.6. In contrast, as stretch rate increases in the simulation, Figures 5.3 and 5.4 show up to a 25% increase in peak O-atom concentration while H-atom concentration is predicted to increase up to 36% in Figure 5.5. This differing trend between prediction and measurement in 2D cellular flames is not understood and merits further investigation. An increase in number density with stretch rate is seen between the dearth regions. Here, the outer portions of the cells move closer together and occupy more of this area leading to higher perceived concentrations.

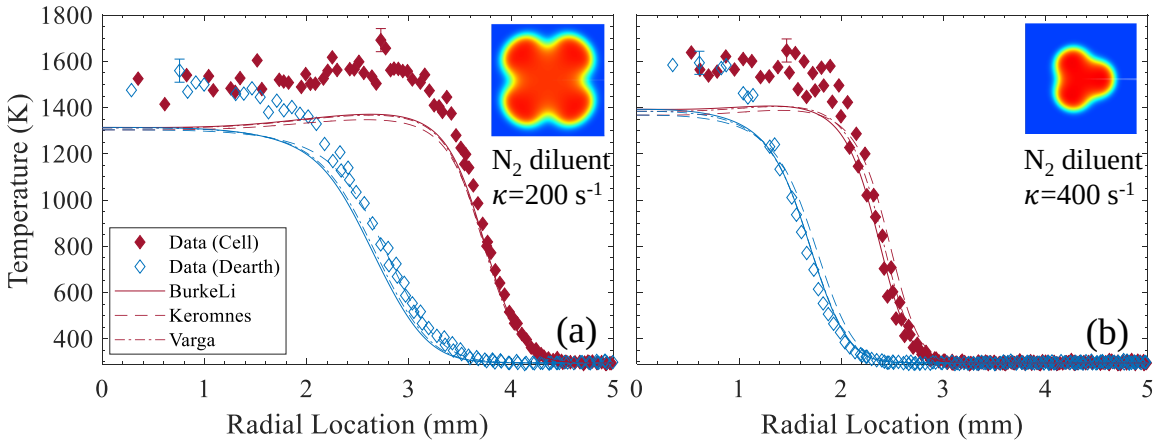

Figure 5.6. Cell and dearth temperature profiles extracted from Fig. 3 and 4 of [16].

Despite higher number densities being predicted for the high-stretch flame of Figure 5.4(b), peak number densities still remain within uncertainty values for the cellular region though concentrations in the dearth region are, once again, over-predicted. Simulated cells for the 400 s^{-1} flame exhibit higher curvature over the low-stretch flame and therefore predict a 25% increase in atomic oxygen concentration. In addition, the profiles are visibly shifted from the data by about 0.5 mm.

Although there is reasonable comparison between data and simulated atomic oxygen, the predicted high-stretch, atomic hydrogen number densities (Figure 5.5) are 15% greater than the upper extent of the error bar. More H-atom continues to be found than predicted in the product zone of the high-stretch flame. The greatest shortcoming in these N_2-diluted tubular flame simulations, however, lies in temperature prediction. This is demonstrated in Figure 5.6 where the Raman-derived temperature measurements are nearly 20% greater than the model. To ensure the temperature data was captured correctly, the Raman scattering measurements were validated against filtered Rayleigh scattering measurements [64].

5.2.2. Replication of atomic hydrogen profiles

While preparing this work on O-atom profiles, the H-atom data of Figure 5.5(a) was also replicated in order to verify the present data reduction method. The experimental setup was kept the same as the present O-atom setup except the OPA was set convert the pump beam to 205 nm to drive the $3d\ ^2D_{3/2,5/2} \leftarrow 1s\ ^2S_{1/2}$ H-atom transition, and a Semrock FF01-655/40-50 band pass filter was used to discriminate the 656 nm de-excitation emission. The maximum pulse energy achieved in this configuration was approximately 2.5 μJ (2.6 mJ/cm^2). This value was lower than the 4.3 μJ of [16], and all of it was used to probe the flame since it was not expected to induce photolytic interference [17]. Data were also reduced in the same way except quenching cross-sections for major quenchers relative to H-atom were used [40].

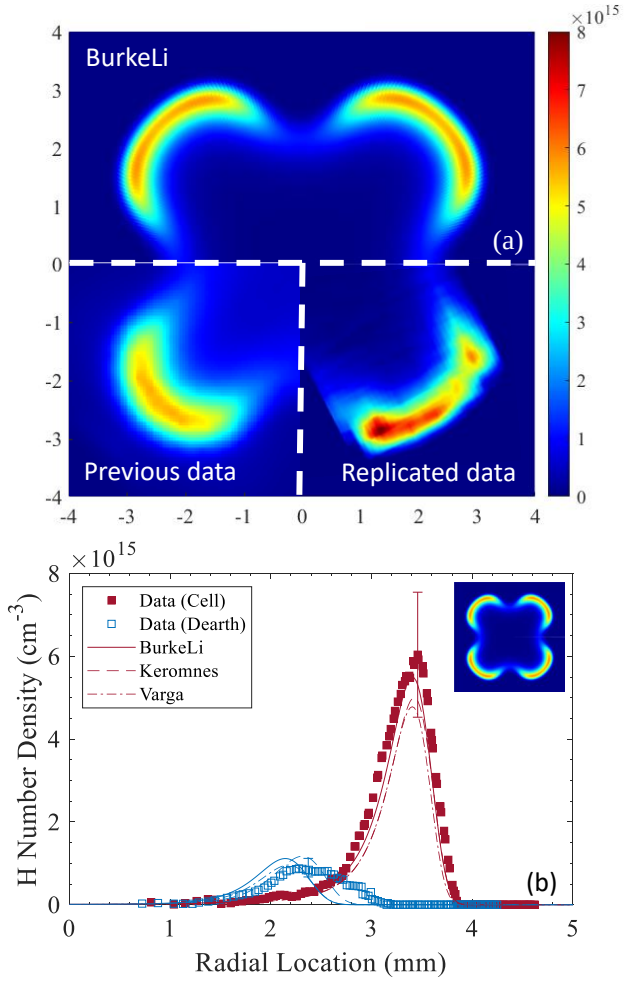

Figure 5.7. Replicated H-atom 2D (a) and 1D (b) profiles for the N_2-diluted, 200 s^{-1} hydrogen flame using the current experimental setup compared to simulation.

The 2D profile of the replicated data in Figure 5.7(a) suffers from the same low-resolution, 0.5 mm step of the burner as the O-atom data, hence the asymmetry. The cell thickness is nonetheless thinner than the atomic hydrogen measurements of the previous study; it is also easier to see that there is no atomic hydrogen present in the product zone of the replicated data in Figure 5.7(b). This could indicate that there may have been photolytic interference present in the previous study which can occur from beam interaction with a number of H-

carrying molecules [17, 58, 65]. Nevertheless, the previous data still appears to have utility in representing peak number densities especially within the cell.

5.2.3. CO_2-diluted flame

Diluent was changed from N_2 to CO_2 to produce the flame in Figure 5.8. Total O-atom concentrations are lower in this configuration due to the presence of CO_2 which becomes chemically active at the elevated flame temperature. The CO radical in particular creates an additional pathway for atomic oxygen consumption through $\mathrm{CO} + \mathrm{O}(+\mathrm{M}) \rightleftharpoons \mathrm{CO_2}(+\mathrm{M})$. The HCO radical consumes O-atoms as well, but is present in much lesser quantities than CO. Under this diluent-equivalence ratio combination, the simulations predict number densities in great excess of the measured values. While past numerical results of 1D, CO_2-diluted tubular flame configurations have agreed with data [14, 50], a similar disparity between data and model to that shown in Figure 5.8 has been observed in other major and minor species profiles of the 2D, CO_2-diluted flame [42].

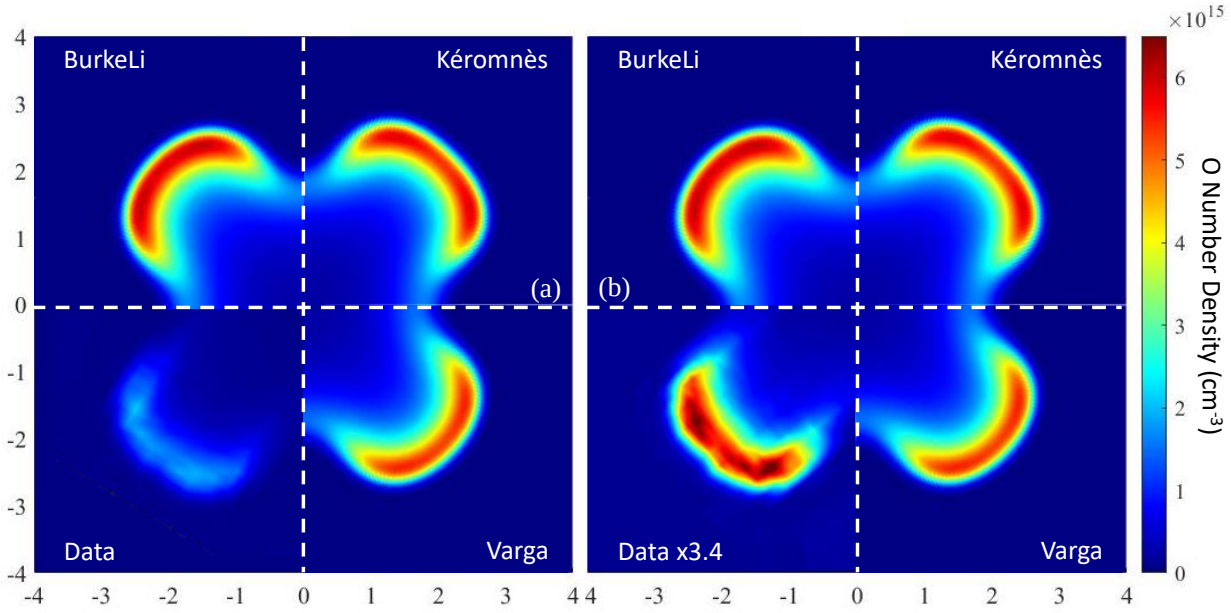

Figure 5.8. Comparison of 2-D profiles between simulations employing various chemical mechanisms and O-atom data for a CO_2-diluted tubular flame with a stretch rate boundary condition of 60 s^{-1}.

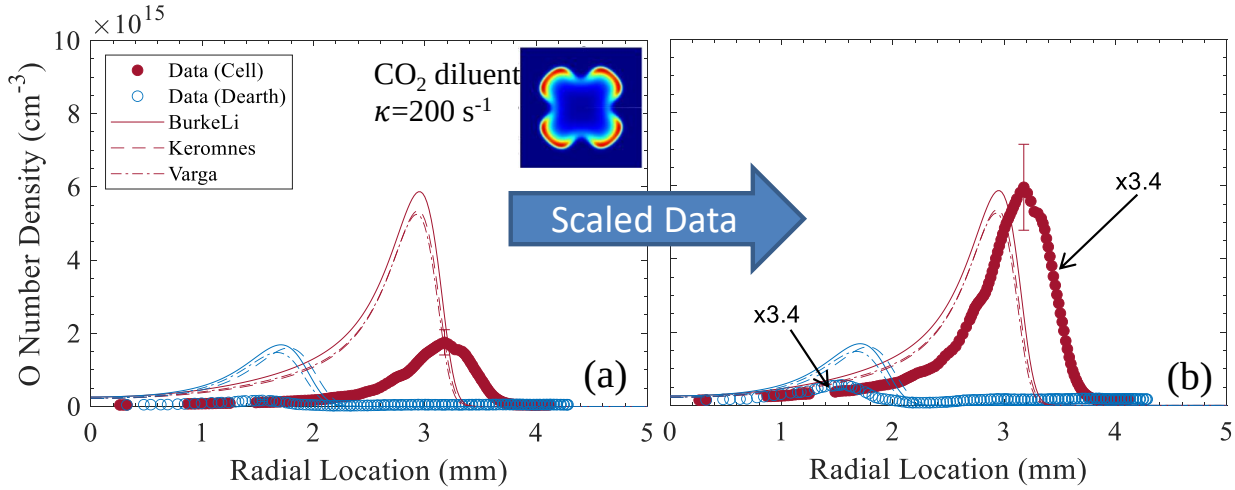

Figure 5.9. Cell and dearth O-atom profiles extracted from Figure 5.8.

Finally, 1D profiles of data and simulations for the κ=200 s^{-1}, CO_2-diluted flame are presented in Figure 5.9. As apparent in the 2D profile, simulated number densities are shown to over predict the peak mean of the data by nearly 340%. Radial location is shifted here as well

and is, again, a similar shift as seen in other simulated minor species profiles with the same value for *W* [42]. Figure 5.9(b) scales the data by 3.4x to show the profiles of Figure 5.9(a) in more detail. Error bars are given in Figure 5.9(b) to show the uncertainty as it relates to the data and should not be related to the accuracy of the simulations.

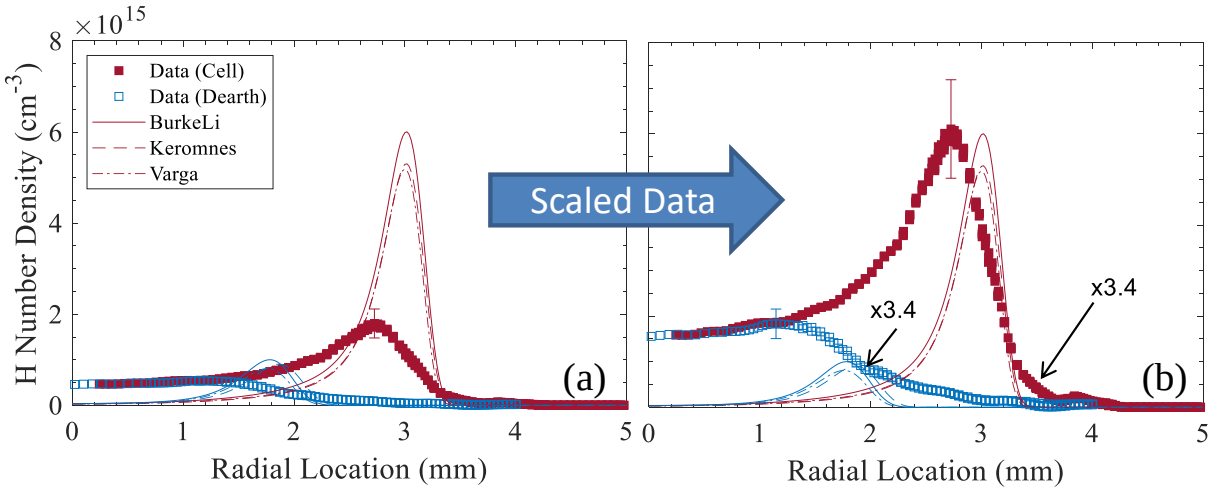

Figure 5.10. Cell and dearth H-atom profiles extracted from Fig. 4.4 of [42].

Measured atomic hydrogen profiles compare similarly to the simulation as they are likewise over-predicted by 340% as seen in Figure 5.10. As before, more H-atom was measured in the product zone than expected. When the data is scaled by 3.4x in Figure 5.10(b), peak number densities are approximately the same between the data and simulation of the cell, but the data profile is much wider than predicted. The dearth region is also too greatly magnified in this case. Despite the model's inaccuracies in generating minor species profiles for these CO_2-diluted flames, temperature is slightly better predicted as seen in Figure 5.11. The simulations better align with the temperature profiles here than in the N_2 diluted case though they slightly over-predict the data.

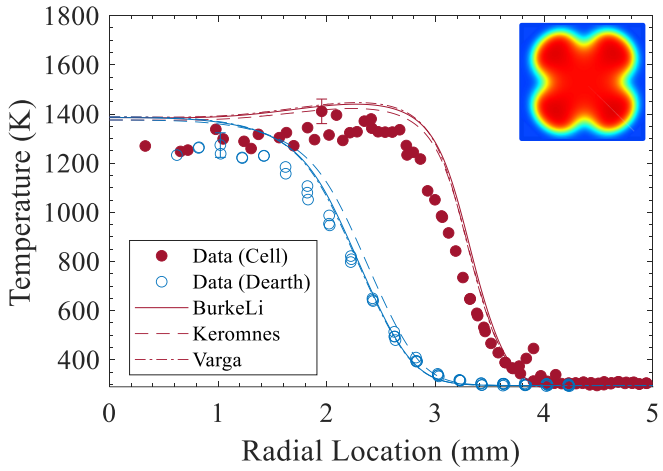

Figure 5.11. Cell and dearth temperature profiles extracted from Fig. 4.4 of [42].

5.2.4. Peak Offsets

Another metric by which to assess flame structure is the difference between the peak locations of the cell and dearth regions. This allows comparison of the relative radial locations of the flames while avoiding any uncertainty in locating the true r=0 in the measurements. Figure 5.12 displays these values for both the data and simulation of O- and H-atom profiles in the tested flame conditions. Peak-offset values are similar between the two atomic species since both radicals depend on high reaction activity to be created and are readily consumed by other species. While all of the proposed mechanisms agree with each other, they under-predict the data-based values by 7–35%.

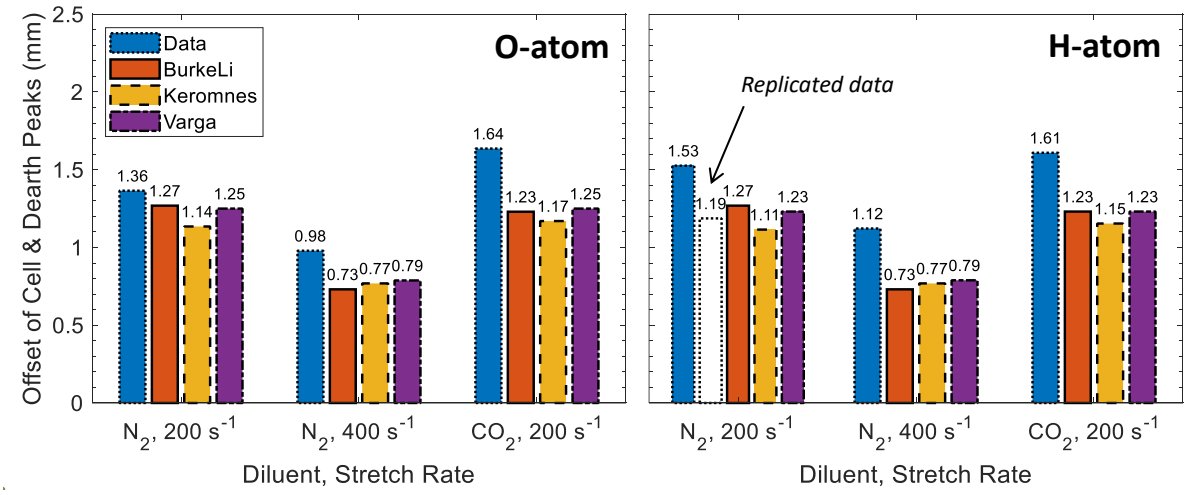

Figure 5.12. Distance between the peaks of the O- and H-atom cell and dearth profiles at the three diluent-stretch flame conditions.

Predicted and measured discrepancies in relative cell and dearth locations in 2D tubular flames, the 200 K temperature difference in N_2-diluted flames, the species concentrations of CO_2 diluted flames, all combined with the mechanisms' ability to *successfully* predict 1D configurations may be pointing to an error in the definition of the flow field. In order to simplify the domain, the boundary layer assumption [11, 42, 44] was applied to relate the axial component of velocity to the radial component and thus reduce the 3D problem to two dimensions. The 1D tubular flames whose maximum studied radii have been <1.25 mm may be well within the boundary layer of the flow field whereas the cells in this work have a minimum radius of 2 mm. However, this value is still small compared to the 12 mm nozzle radius. Another theory is that the nozzle height of 8 mm is not large enough to avoid three-dimensional effects on the flame. Thus, it could prove beneficial to perform 3D DNS in order to assess disparities, if any, between the model definitions.

5.3. Conclusions

Quantitative measurements of atomic oxygen have been obtained in premixed, H_2/O_2 2D tubular flames diluted with N_2 or CO_2 at relatively low- and high-stretch rates. Femtosecond TALIF scans of the flames along with previously captured Raman scattering data for temperature and major species (H_2, O_2, H_2O, N_2/CO_2) were combined using a temperature-dependent calibration to produce the 2D O-atom profiles. Past research has found simulated profiles to adequately predict major and minor species data for 1D tubular flames [14, 50]. However, there are shortcomings associated with predicting the 2D cellular flame configuration. For instance, the minor species number density profiles are predicted to increase with stretch rate though the peak measured values remain constant. While there is still reasonable agreement between profiles of measured and simulated 2D flames diluted with N_2, the flame diluted with CO_2 continues to be difficult to predict as computed profiles suggest a 340% greater presence of O-atom than is measured. This trend has also been observed in past minor species measurements for CO_2 diluted flames [42].

Minor species, like atomic oxygen, are sensitive to changes in transport and kinetic properties making them an attractive target for evaluating the performance of chemical mechanisms. The three mechanisms employed here to simulate the tubular flames were those created/modified by Burke *et al*. + Li *et al*. (BurkeLi) [51, 52], Kéromnès *et al*. [53], and Varga *et al*. [54]. All three mechanisms performed comparably to one another in all flames for both cell and dearth regions. Since these mechanisms were effective at computing 1D, lean H_2 flames diluted with N_2 or CO_2, the error associated with the predictions of the 2D flames is hypothesized to have resulted from an invalid boundary layer assumption. The simplifying assumption that relates the axial component of velocity to radial velocity may apply to 1D flames

whose radii are smaller while the 2D flames shown here may lie outside of the boundary layer. If this is true, the current simulations may be applying an incorrect local stretch value near the flame zone which could lead to the flame structure discrepancies against the data.

Atomic oxygen plays an important role in turbulent simulation [19, 20]; thus accurate modeling, chemical kinetic, and transport properties for such a radical are essential for more precise turbulent flame predictions. Isolating and correcting inaccuracies will allow for a more confident assessment of full and reduced chemical mechanisms across a range of fuels and flame configurations. The increased fidelity could, in turn, offer more insight into imprecisions associated with simulating turbulent combustion. Future research will explore the effects of standard flow field simplifications, particularly the boundary layer assumption that relates the radial and axial velocities in the flow stagnation zone, on tubular flame structure.

CHAPTER 6

6. HEAT RELEASE INDICATORS FOR H_2-AIR FLAMES

This chapter is adapted from "Evaluation of heat release indicators in lean premixed H_2/Air cellular tubular flames" published in the *Proceedings of the Combustion Institute* and has been reproduced with the permission of the publisher and my co-author Robert W. Pitz [9].

6.1. Proposed Tracer Quantities for Heat Release

To date major species H_2, O_2, N_2, and H_2O as well as OH, H, O, and OH* (electronically excited OH) minor species have been measured in H_2-air tubular flames of various configurations [13, 16, 50, 66, 67] making them primary candidates for this study. Since N_2 does not significantly contribute to the overall heat release of the flame, it is excluded. According to the kinetic model for H_2/O_2 combustion by Burke et al. [51], H_2O is not present in many reactions that would strengthen heat release through radical production. Those reactions in which H_2O exists with radicals often involve three bodies making them slower than other heat producing reactions. One exception is the $OH + H_2 \Leftrightarrow H_2O + H$ equilibrium reaction. Here, the reverse reaction to remove H_2O is much slower than the forward reaction at flame temperatures (~1400 K). Subsequent reactions slowly remove H_2O in the mechanism. Thus, $[H_2O]$ is also excluded as a stand-alone tracer and from any potential combinations.

This leaves H_2, O_2, OH, H, O, and OH* to be studied either singly or combined. Intuition and previous studies suggest that $[H_2]$ and $[O_2]$ will not be sufficient in themselves to mark the flame zone as both are primarily consumed throughout the reaction. H_2 consumption begins before the area of greatest heat release, and little of the deficient reactant exists in the product

zone for lean flames. [OH] may be capable of indicating the onset of heat release, but it exists in large quantities on the product side of the overall reaction compared to other species causing it to over-predict the flame width. As previously mentioned, [OH*] has been used historically to study flame zones because of its rapid creation and de-excitation and will be considered in the current study. Atomic hydrogen will also be considered because of its high reactivity.

The reactions that contribute most to heat release are: $H + O_2 \rightarrow O + OH$, $O + H_2 \rightarrow H + OH$, and $OH + H_2 \rightarrow H_2O + H$ as suggested by Goodings and Hayhurst [31] and implied by the Burke mechanism [51]. Goodings and Hayhurst also note the importance of the $OH + OH \rightarrow H_2O + O$ reaction in fuel-lean systems; however, because the reaction rate coefficients for its forward and backward reactions are much less than those of the other reactions at high and low temperatures, a combination of these species will not be considered. Therefore, the combinations that will be considered are $[O_2]x[H]$, $[OH]x[H_2]$, and $[O]x[H_2]$.

Nine single species and sixteen combinations were considered in the preliminary search for an HRR indicator and are listed in Table 6.1. Of these, the five tracers discussed above were found to have the best potential merit, and are analyzed in the results below.

Table 6.1. List of tracers considered in preliminary study. Highlighted cells showed the most merit and are further studied in this paper.

$[O]$	$[H]$	$[H_2]$	$[H_2O]$	$[H_2O_2]$
$[HO_2]$	$[O_2]$	$[OH]$	$[OH^*]$	$[H]x[H_2]$
$[H]xTemp$	$[H]x[O]$	$[H]x[H_2O]$	$[OH]x[HO_2]$	$[OH]x[O]$
$[OH]x[O_2]$	$[OH]x[H_2]$	$[OH]x[H_2O]$	$[OH^*]x[H_2]$	$[OH^*]x[O_2]$
$[O]x[H_2]$	$[O_2]x[H]$	$[OH^*]x[H_2O]$	$[OH^*]x[H]x[H_2O]$	$[H_2]x[H]^2xTemp$

6.2. Numerical Simulation Details

Two-dimensional DNS was carried out using the code developed by Hall and Pitz [11]. Chemical kinetics along with thermal and transport property values were taken from the Burke mechanism [51] because of its reasonable accuracy in reproducing previously recorded species data [11]. For H_2-air flames, this mechanism includes 19 reversible reactions, 8 reacting species (H_2, O_2, H_2O, H, O, OH, HO_2, H_2O_2), and 1 non-reacting species (N_2). The Burke mechanism was found to best predict the tubular flame structure in regions of high and low reactivity based on a comparison to major species (H_2O, H_2, O_2) and minor species (H, OH) data acquired by Raman scattering and LIF respectively [11, 16].

Preliminary studies in a non-cellular flame were conducted to determine suitable combinations of species concentrations to mark the reaction. Results suggested the applicability of [OH*], [H], $[O_2]$x[H], [OH]x$[H_2]$, and [O]x$[H_2]$ for tracking heat release rate in non-cellular tubular flames. The tracer combinations [H] and $[O_2]$x[H] were subsequently applied to experimentally measured 2D, cellular flames (with [H] and $[O_2]$ data) to predict HRR profiles.

6.3. Results

Cellular flames were simulated under stretch rates of 200 s^{-1} and 400 s^{-1} forming four and three cells, respectively, to determine the robustness of the chosen species as stretch rate varied. The heat release rate is shown in Figure 6.1 for both cases. The normalized profiles show unique regions of high reactivity (maximum heat release) as cells separated by zones of low reactivity. Such regions are formed by the preferential diffusion of the deficient reactant, hydrogen, in these $Le < 1$ flames. Smaller local radii of positive (convex) curvature increases local flame temperature and flame speed to stabilize the cells.

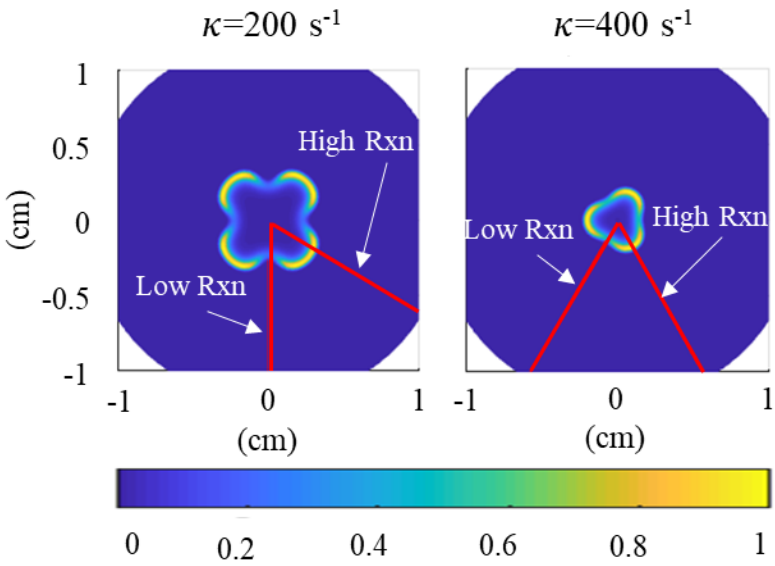

Figure 6.1. Calculated, normalized HHR for H_2-air flames of Φ=0.25. Subsequent plots are shown with respect to the red lines.

Planar profiles of the considered species are qualitatively similar to the HRR shown in Figure 6.1. Figure 6.2 shows a quantitative look at the calculated species data compared to the HRR in high- and low-reactivity zones. All of the proposed tracers appear to relate well to HRR in the zones of increased reaction both in terms of magnitude and location for either stretch rate; however, there is an apparent offset between the magnitudes in the lower reactivity zones. Here, [OH*] begins to indicate a lack of flame presence in both conditions though the HRR suggests otherwise as shown in (b) and (d) of Figure 6.2.

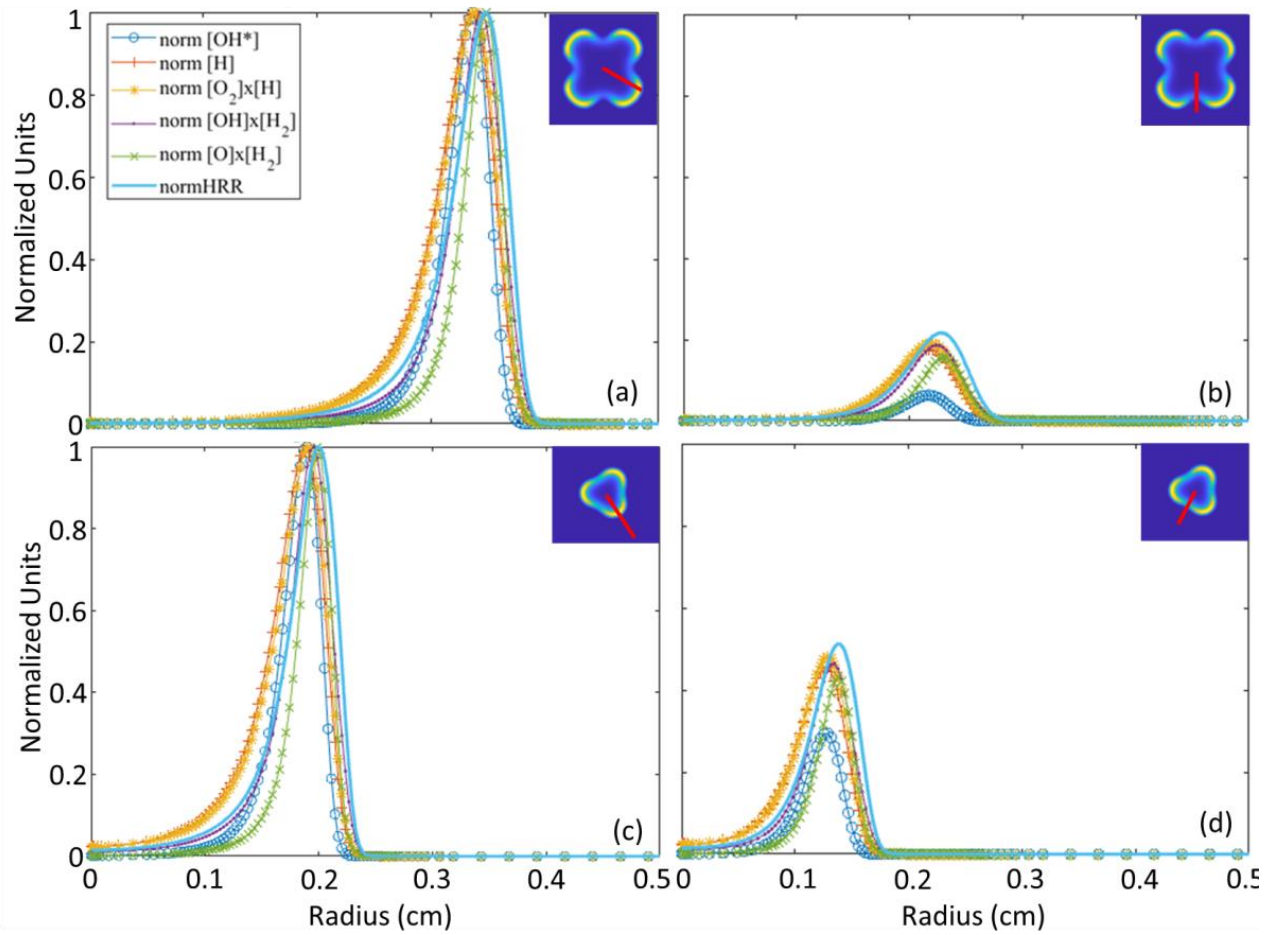

Figure 6.2. Normalized profiles of individual species and species products.

Because the profiles are so closely aligned, it is difficult to distinguish between the tracers' accuracies. Thus, it is often more informative to plot the concentration profiles against HRR as shown in Figure 6.3 since this relationship is more sensitive to spatial discrepancies [68]. A tracer with a perfect match to HRR would appear as a rising diagonal line from zero to one. The upper surface of these curves compare the alignment of a species' leading edge with HRR while the lower surface compares the trailing edge. In Figure 6.3, [OH*] appears to match HRR the least in both the high and low reactivity regions of each cellular case. Concentrations of H and O_2xH are very closely related with the latter performing insignificantly better.

Finally, the best tracers suggested by these plots are [OH]x[H_2] and [O]x[H_2]. Between these, the center of the [O]x[H_2] curve aligns directly with the center location of HRR while predicting the leading edge well. [OH]x[H_2] better predicts the width of the HRR profile thus tracing both the leading and trailing edges more accurately.

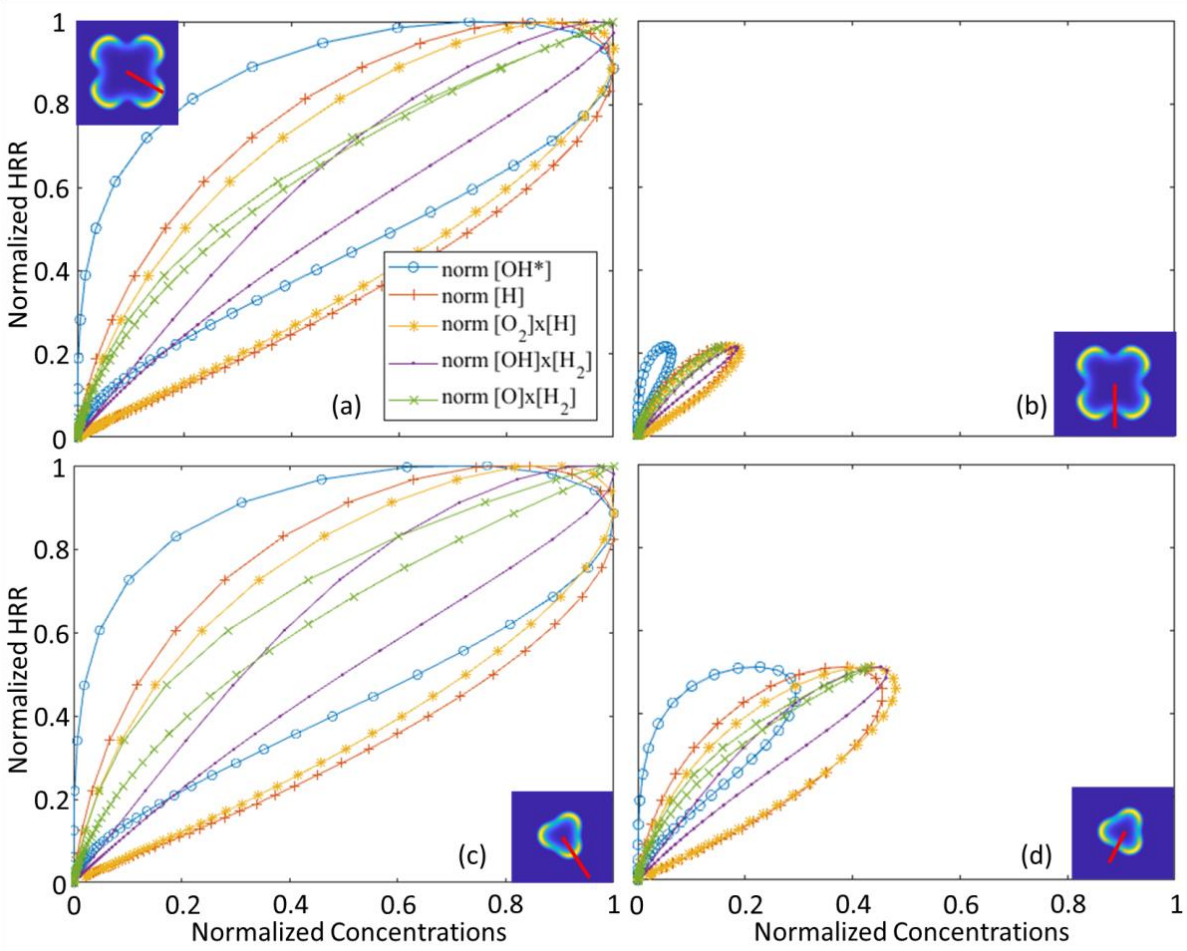

Figure 6.3. Normalized values for calculated HRR vs. normalized, simulated concentrations for the high and low reactivity regions of the flames.

One may also choose to examine the differences based on each individual parameter as in Table 6.2. “Magnitude” compared the normalized, maximum amount of heat release, “center” compares the location of the maximum amount of heat release, and “FWHM” compares the full-

width at half-maximum of the heat release profiles to a given tracer. Most of the parameters are similar between the species with the exception of magnitude determined by [OH*] in the low reactivity regimes. In these instances, [OH*] greatly under-represents the HRR.

Table 6.2. Offset values comparing tracers to HRR. Negatives indicate a lesser property value than HRR.

4 CELL REGION:	High Reactivity			Low Reactivity		
Tracer	Magnitude % diff	Center % diff	FWHM % diff	Magnitude % diff	Center % diff	FWHM % diff
[OH*]	0.0	-3.5	-27.3	-71.0	-5.3	-21.4
[H]	0.0	-3.5	9.1	-18.7	-5.3	-7.1
$[O_2]x[H]$	0.0	-2.6	-36.4	-12.2	-4.0	-7.1
$[OH]x[H_2]$	0.0	-1.7	-27.3	-14.0	-2.7	-28.6
$[O]x[H_2]$	0.2	0.0	-54.5	-28.5	0.0	-35.7

Unacceptable Acceptable

3 CELL REGION:	High Reactivity			Low Reactivity		
Tracer	Magnitude % diff	Center % diff	FWHM % diff	Magnitude % diff	Center % diff	FWHM % diff
[OH*]	0.0	-4.6	-11.1	-42.5	-6.7	-44.4
[H]	0.0	-4.6	22.2	-11.3	-6.7	22.2
$[O_2]x[H]$	0.0	-4.6	11.1	-6.2	-6.7	11.1
$[OH]x[H_2]$	0.0	-1.5	-11.1	-9.4	-2.2	-11.1
$[O]x[H_2]$	0.0	0.0	-33.3	-16.0	0.0	-44.4

Data published by Hall and Pitz [11] may be compared to the *simulated* HRR as shown in Figure 6.4. Atomic hydrogen concentrations as well as its pixel-by-pixel multiplication with O_2 concentrations show little difference as was predicted by the numerical results. The data does not seem to compare to HRR as well as anticipated especially in regions of low reactivity. If the model better predicted the species profiles, the HRR between the concentration data and simulation would be expected to align within 10%. Offset properties of the data from the

simulated HRR are quantized in Table 6.3. Adding data for [OH*] profiles would aid in determining its worth against [H] but is currently unavailable.

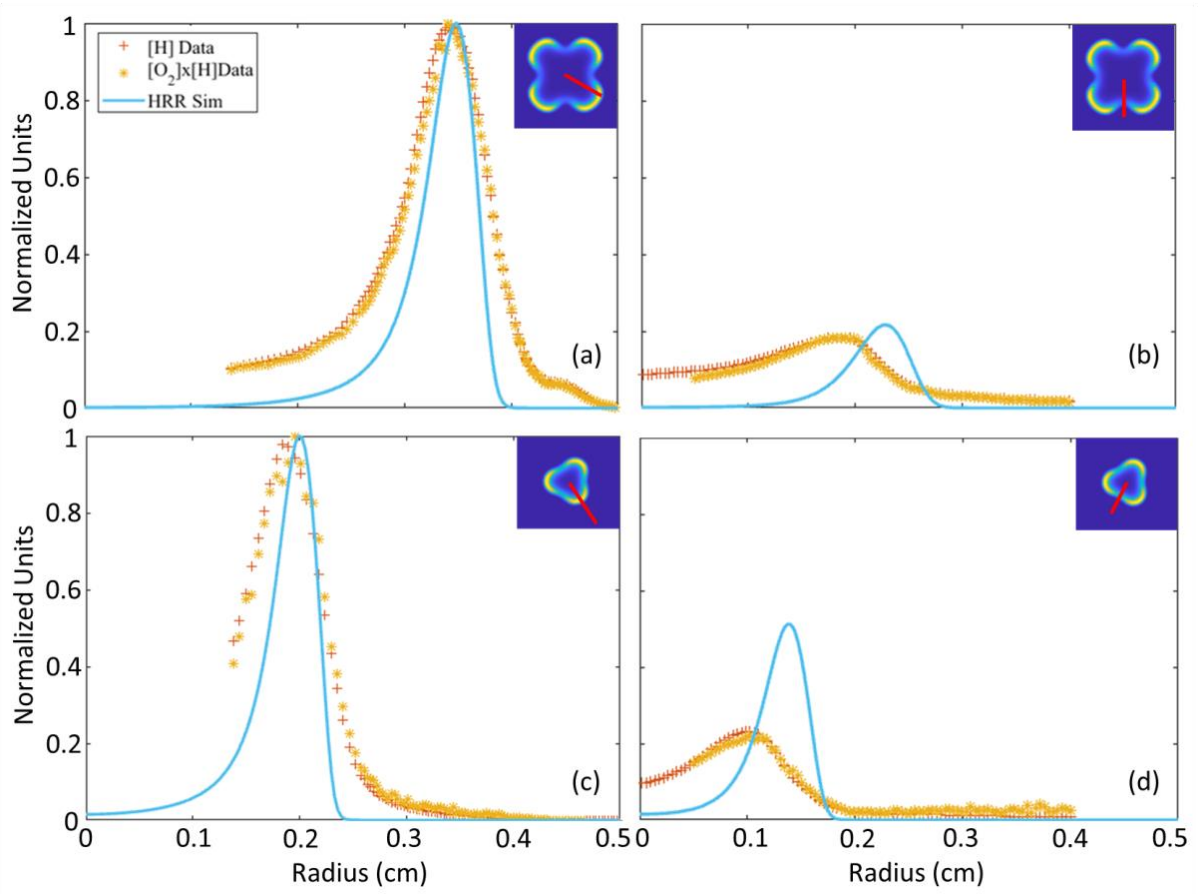

Figure 6.4. Comparison of experimental [H] and $[O_2]$x[H] [11] against calculated HRR.

Table 6.3. Offset values between data profiles and simulated HRR. Negatives indicate a lesser property value than HRR.

	High Reactivity			Low Reactivity		
Tracer	Magnitude % diff	Center % diff	FWHM % diff	Magnitude % diff	Center % diff	FWHM % diff
4-cell [H]	-1.1	-2.4	25.8	-16.1	-18.6	-13.3
3-cell [H]	0	-4.8	49.0	-55.1	-25.6	33.8

In all of the presented cases, experimental results err towards the center of the flame though to a greater extent than the simulated results. Moreover, the data is also consistent with the simulation insofar as the flame width is overestimated though, again, to a greater degree. Higher quantities of [H] and $[O_2]$x[H] are seen in the product side of the flame than expected creating difficulty in defining the width of the data. Since this is true for both profiles, any major error related to experimentation may be due to interference during H-atom LIF. However, the DNS code may also require more tuning to better represent these cellular flames. Finally, without knowing the actual, absolute concentrations of all major species in the experimental flame, the simulated HRR is only a best-guess at actual flame conditions.

6.4. Discussion

Increasing stretch slightly improves the comparative values of each species combination – the [OH*] profile benefiting the most. This could be caused by increased proximity of the low reactivity zone to the high reactivity zone thus increasing OH* production. Temperature in the low reactivity region increases by ~100 K from 200 to 400 s^{-1} stretch rate. Stretch conditions do not appear to substantially affect the ranking of species accuracy between the 200 and 400 s^{-1} cases; therefore, the following discussion will be independent of stretch.

OH* is produced as OH $A^2\Sigma$ and is the easiest excited state of OH to be measured as 2D images may be captured from chemiluminescence in the UV range. The above results suggest, however, that OH* may not be a good indicator of flame extinction.

$[O_2]$x[H] follows HRR with slightly more accuracy than [H]. Any improved performance of $[O_2]$x[H] might be attributed to its dual presence within the reaction mechanism. When this combination appears as a reactant, it releases heat in the high temperature regime

where O and OH radicals are produced as well as the low temperature regime where the HO_2 radical continues the reaction. However, the difference is not significant enough as suggested by the numerical and experimental results to justify the added measurement complexity. The hydrogen atom exhibits high performance as expected since it is produced during the chain initiation step and is quickly removed across the flame zone due to its high reactivity. Measurement of this species is most often conducted using two-photon LIF [14, 17, 57, 59]. H atoms are excited at 205 nm for the n = 1→→3 transition while fluorescence is collected from the n = 2←3 transition at 656 nm. Such a process requires pulses in the pico- to femtosecond regimes in order to reduce/eliminate photolytic interference. Due to low H concentrations in these lean flames, further research is required to measure a planar profile – a necessity for [H] to trace HRR in turbulent flows.

Atomic oxygen similarly requires two-photon LIF in the femtosecond regime for accurate measurement [37, 38, 50]. Oxygen atoms are excited at 225 nm for the n = 1→→3 transition while fluorescence is collected from the n = 2←3 transition at 844 nm. Again, planar imaging is difficult because of such low quantities making application to turbulent conditions difficult. When [O] is multiplied by [H_2], it still does not describe the reaction zone well enough to justify the complexity of the measurement method. It does, however, align perfectly with the HRR. This could suggest it has the greatest impact on the magnitude of HRR in the Burke mechanism.

Both OH and H_2 have each been extensively measured [7, 13, 16, 24, 68]. Planar imaging of the OH radical is possible with a tunable laser set to ~285 nm while capturing a UV signal within 300–340 nm. The process involves a single photon excitation of the $A^2\Sigma^+ \leftarrow X^2\Pi(1,0)$ $Q_1(5)$ line. More simply, one could infer the amount of OH from chemiluminescence of OH* in H_2-air flames if a valid chemical mechanism for OH production/destruction is assumed.

Molecular hydrogen is often quantified by point (or line) measurement via spontaneous Raman scattering. Turbulent profiles of Raman-collected species have been captured by refocusing a beam between two cylindrical lenses forming 2D images [69]. If carefully applied, simultaneous capture of [OH] and [H_2] may be possible; however, this may also be too complex for the slight increase in HRR resolution.

6.5. Conclusions

[OH*], [H], [O_2]x[H], [OH]x[H_2], and [O]x[H_2] have been computationally compared for their ability to describe the heat release zone in lean, premixed H_2-air tubular flames. The tubular geometry allowed the proposed tracers to be assessed in regions of both high and low reactivity for stretch rates of 200 s^{-1} and 400 s^{-1}. Results indicate that [OH*] describes the reaction zone well enough in the high heat release region, but may suggest an early extinction as related to spatial coordinates.

Overall, the tracers experienced slight improvement in comparative values with increased stretch rate. This may be caused by a decrease in tubular flame diameter thus increasing the proximity between the high and low regions of reactivity to further drive the chemical reactions. [OH]x[H_2] best predicts the HRR considering the magnitude, peak offset, and width differences. While OH distributions have been captured using planar LIF, it is difficult to acquire planar measurements of H_2. Thus, application to turbulent flows is not currently possible. [O]x[H_2] best predicts the center location of HRR, but lacks in its description of magnitude and width. The complexity required for this measurement, therefore, renders no advantage. Finally, [O_2]x[H] and [H] profiles performed comparably. However, improvements in planar measurements of [H] may allow the simplest and most accurate measurement of HRR in H_2-air premixed flames.

CHAPTER 7

7. CONCLUSIONS

This work has been conducted to three ends: 1) to further expand the knowledge of radical behavior in the presence of flame stretch and curvature by measuring atomic oxygen in tubular flames, 2) to compare contemporary hydrogen chemical kinetic mechanisms against measurements of the sensitive O-atom, minor species, and 3) to re-examine heat release markers for hydrogen combustion while proposing more accurate alternatives.

To meet the first two goals, quantitative atomic oxygen measurements in high- and low-stretch rate tubular flames diluted with N_2 or CO_2 in both non-cellular and cellular configurations were obtained using fs-TALIF signal quench corrected from Raman measurements. Not only were species profiles determined, but the calibration process was also more fully scrutinized than past endeavors. Quenching effects were shown to be imperative to consider in both the calibration and data reduction operations when the composition and temperature of the calibration and experimental flames differed. Simulated profiles agreed best with the data, however, when temperature-dependent quenching of H_2O was also included. All tested chemical mechanisms predicted O-atom profiles within the uncertainty of the data and comparably predicted the profile geometries in all of the non-cellular flames studied.

Qualitatively, simulated 2D O-atom profiles in N_2 diluted tubular flames compared well with data for all examined mechanisms. Simulated profiles through the cellular region of the flames showed good agreement with the data for all chemical mechanisms as they were captured by data uncertainty. However, concentrations in the dearth regions are over-predicted for O-atom despite capturing H-atom concentrations well in this region.

As stretch rate increased, the experimental flame cells simply shifted radially while their radius of curvature remained unchanged. Thus, peak number densities in the cells were constant between the flames. Measured dearth concentrations increased slightly as the cells drew closer together. However, the simulated flames were not only found to have increased O- and H-atom concentrations in the dearth region, but concentrations within the cells also increased. This was due to an incorrect prediction of a decrease in the cells' curvature leading to local reaction enhancement.

When the low stretch flame was diluted with CO_2, measured quantities of O-atom (and H-atom) were much lower than predicted. This continues to follow the trend of other minor species measurements in the presence of flame stretch and curvature. Neither the Kéromnès, *et al.* nor Varga, *et al.* mechanisms approached measured number densities but were instead comparable to the legacy kinetics of Burke, *et al.* + Li, *et al*. carbon pathways.

Heat release tracers [H], $[O_2]$x[H], [OH]x$[H_2]$, and [O]x$[H_2]$ were computationally compared against commonly used [OH] and [OH*] tracers for their ability to describe the heat release zone in hydrogen combustion. Results indicate that [OH*] adequately describes the reaction zone in the high heat release region, but may predict extinction too early as related to spatial coordinates while [OH] is too slowly removed to quickly respond to HRR depletion.

Overall, the tracers' performances in mapping high-reactivity regions were comparable as stretch rate increased. Of the tracers, [OH]x$[H_2]$ best modeled the HRR in terms of predicting magnitude, locating peak values, and determining FWHM. This combination is not expected to perform well in rich locales, however, as excess H_2 would be present in the products leading to over-prediction of HRR. Normalized profiles of [H] were also shown to trace heat release zones well and could be expected to perform well in both rich and lean conditions. Improvements in

planar measurements of [H] may allow the simplest and most accurate measurement of HRR in H_2-air premixed flames.

7.1. Suggestions for Future Work

This work has built upon others to contribute knowledge of minor species behavior in stretched and curved flamelets. In the current state, non-cellular flames are very well predicted by 1D simulations. However, the discrepancy between simulated and measured cellular, tubular flames is still not well understood.

The primary concern is the slight inconsistency in major species and the drastic over-prediction of minor species in CO_2 diluted flames. Two possible causes for this are 1) inaccurate chemical kinetics and transport properties and 2) inaccurate flow field modeling.

The first cause is unlikely since the non-cellular flames are well-predicted; however, studying flames similar to the ones presented using other diluents (e.g. He and Ar) would help determine if CO_2 itself is causing the discrepancy. For instance, it may be possible that CO_2's participation in reactions of the dearth region is not being completely captured. Capturing minor species CO profiles in the CO_2-diluted flame would also aid in the understanding of the chemistry in different regions of these flames.

Inaccurate modeling of the flow field is the most likely culprit for the poor performance in predicting the CO_2-diluted flame. One thought is that the boundary layer assumption that reduces the 3D problem to 2D is not valid for flames of a certain radius. This radial limit may be greater than those of the non-cellular flame radii (1.5 mm) which could explain their model accuracies. To test this, simulated, non-cellular hydrogen flames of larger radii (lower stretch rate) could be measured. Another approach would be to perform 3D DNS of the flames. This

would not only inform use of the boundary layer assumption, but would also uncover any influence of the nozzle's height on the axial distribution of species.

The N_2-diluted flames are not without their shortcomings either. Neither of the modified/optimized reaction mechanisms explored herein minimized the 200 K temperature error associated with modelling cellular flames using the BurkeLi mechanism. This could, once again, be influenced by flow field assumptions since temperature distributions in non-cellular flames have been well-predicted. An adjacent issue is the model's inability to reproduce the constant flame curvature of the data. As stretch rate increases in the current model, temperature and species profiles increase through curvature enhancement. However, the data shows that only the radial location of and number of the cells change keeping peak temperature and minor species concentration constant. These inconsistencies would also benefit from the knowledge provided by 3D DNS simulations of these reacting environments.

This work has provided insight into minor species within premixed tubular flames. Other configurations such as non- and partially-premixed flames have been modelled with reasonable accuracy though H_2O and in some instances temperature have strayed significantly for certain flames [66, 70]. The configurations would also benefit from minor species studies to identify which intermediates are being poorly captured leading to the error in water prediction.

Finally, analytical or empirical models of the stretch rate boundary condition for various gas mixtures would increase confidence that the desired flame is correctly simulated. To date, this value has been selected based on aligning temperature and major species profiles between simulation and data. Its value has been shown to change with gas mixture through this method. Accurate prediction of minor species concentrations is dependent on this boundary condition [71]. While hot-wire anemometry could help inform this value, it may be necessary to use a

particle imaging velocimetry or molecular tagging velocimetry technique for accurate quantification.

REFERENCES

[1] S. Li, Y. Ge, X. Wei, T. Li, Mixing and combustion modeling of hydrogen peroxide/kerosene shear-coaxial jet flame in lab-scale rocket engine, Aerosp. Sci. Technol. 56 (2016) 148–154.

[2] T. M. Nguyen, P. P. Popov, W. A. Sirignano, Longitudinal combustion instability in a rocket engine with a single coaxial injector, J. Propuls. Power 34 (2) (2018) 354–373.

[3] N. Peters, Turbulent Combustion, Cambridge University Press, Cambridge, UK, 2000.

[4] A. N. Lipatnikov, J. Chomiak, Molecular transport effects on turbulent flame propagation and structure, Prog. Energy Combust. Sci. 31 (1) (2005) 1–73.

[5] N. Peters, Laminar flamelet concepts in turbulent combustion, Symp. Combust. 21 (1) (1986) 1231–1250.

[6] Y. Xuan, G. Blanquart, M. E. Mueller, Modeling curvature effects in diffusion flames using a laminar flamelet model, Combust. Flame 161 (5) (2014) 1294–1309.

[7] H. N. Najm, P. H. Paul, C. J. Mueller, P. S. Wyckoff, On the adequacy of certain experimental observables as measurements of flame burning rate, Combust. Flame 113 (1998) 312–332.

[8] P. H. Paul, H. N. Najm, Planar laser-induced fluorescence imaging of flame heat release rate, Proc. Combust. Inst. 27 (1998) 43–50.

[9] G. J. Marshall, R. W. Pitz, Evaluation of heat release indicators in lean premixed H_2/Air cellular tubular flames, Proc. Combust. Inst. 37 (2) (2019) 2029–2036. doi.org/10.1016/j.proci.2018.06.046

[10] J. Schlup, G. Blanquart, Validation of a mixture-averaged thermal diffusion model for premixed lean hydrogen flames, Combust. Theory Model. 22 (2) (2018) 264–290.

[11] C. A. Hall, R. W. Pitz, Numerical simulation of premixed H_2-air cellular tubular flames, Combust. Theory Model. 20 (2) (2016) 328–348.

[12] S. Hu, P. Wang, R. W. Pitz, A structural study of premixed tubular flames, Proc. Combust. Inst. 32 (1) (2009) 1133–1140.

[13] D. M. Mosbacher, J. A. Wehrmeyer, R. W. Pitz, C. J. Sung, J. L. Byrd, Experimental and numerical investigation of premixed tubular flames, Proc. Combust. Inst. 29 (2002) 1479–1486.

[14] C. A. Hall, W. D. Kulatilaka, J. R. Gord, R. W. Pitz, Quantitative atomic hydrogen measurements in premixed hydrogen tubular flames, Combust. Flame 161 (11) (2014) 2924–2932.

[15] C. A. Hall, R. W. Pitz, Major species investigation of non-premixed cellular tubular flame, in 54th AIAA Aerospace Sciences Meeting AIAA 2016-1203, San Diego, CA, 2016.

[16] C. A. Hall, W. D. Kulatilaka, N. Jiang, J. R. Gord, R. W. Pitz, Minor-species structure of premixed cellular tubular flames, Proc. Combust. Inst. 35 (2015) 1107–1114.

[17] W. Kulatilaka, J. Gord, V. Katta, S. Roy, Photolytic-interference-free, femtosecond two-photon fluorescence imaging of atomic hydrogen, Opt. Lett. 37 (15) (2012) 3051–3053.

[18] H. U. Stauffer, W. D. Kulatilaka, J. R. Gord, S. Roy, Laser-induced fluorescence detection of hydroxyl (OH) radical by femtosecond excitation, Opt. Lett. 36 (10) (2011) 1776–1778.

[19] Y. Ju, T. Niioka, Reduced kinetic mechanism of ignition for nonpremixed hydrogen/air in a supersonic mixing layer, Combust. Flame 99 (2) (1994) 240–246.

[20] J. H. Tien, R. J. Stalker, Release of chemical energy by combustion in a supersonic mixing layer of hydrogen and air, Combust. Flame 130 (2002) 329–348.

[21] W. D. Kulatilaka, S. Roy, N. Jiang, J. R. Gord, Photolytic-interference-free, femtosecond, two-photon laser-induced fluorescence imaging of atomic oxygen in flames, Appl. Phys. B Lasers Opt. 122 (26) (2016) 1–7.
[22] C. J. Mueller, J. F. Driscoll, D. L. Reuss, M. C. Drake, Effects of unsteady stretch on the strength of a freely-propagating flame wrinkled by a vortex, Proc. Combust. Inst. 26 (1996) 347–355.
[23] D. Fernández-Galisteo, A. L. Sánchez, A. Liñán, F. A. Williams, The hydrogen-air burning rate near the lean flammability limit, Combust. Theory Model. 13 (4) (2009) 741–761.
[24] B. O. Ayoola, R. Balachandran, J. H. Frank, E. Mastorakos, C. F. Kaminski, Spatially resolved heat release rate measurements in turbulent premixed flames, Combust. Flame 144 (1–2) (2006) 1–16.
[25] N. Swaminathan, R. Balachandran, G. Xu, A. P. Dowling, On the correlation of heat release rate in turbulent premixed flames, Proc. Combust. Inst. 33 (1) (2011) 1533–1541.
[26] J. Kariuki, A. Dowlut, R. Yuan, R. Balachandran, E. Mastorakos, Heat release imaging in turbulent premixed methane–air flames close to blow-off, Proc. Combust. Inst. 35 (2) (2015) 1443–1450.
[27] L. Lv, J. Tan, J. Zhu, Visualization of the heat release zone of highly turbulent premixed jet flames, Acta Astronaut. 139 (2017) 258–265.
[28] Z. M. Nikolaou, N. Swaminathan, Heat release rate markers for premixed combustion, Combust. Flame 161 (12) (2014) 3073–3084.
[29] C. Chi, G. Janiga, A. Abdelsamie, K. Zähringer, T. Turányi, D. Thévenin, DNS study of the optimal chemical markers for heat release in syngas flames, Flow, Turbul. Combust. 98 (4) (2017) 1117–1132.
[30] N. T. Clemens, P. H. Paul, Effects of heat release on the near field flow structure of hydrogen jet diffusion flames, Combust. Flame 102 (1995) 271–284.
[31] J. M. Goodings, A. N. Hayhurst, Heat release and radical recombination in premixed fuel-lean flames of $H_2 + O_2 + N_2$, J. Chem. Soc. 84 (6) (1988) 745–762.
[32] B. Karlovitz, D. W. Denniston, D. H. Knapschaefer, F. E. Wells, Studies on turbulent flames, Proc. Combust. Inst. 4 (1953) 613–620.
[33] P. Wang, J. A. Wehrmeyer, R. W. Pitz, Stretch rate of tubular premixed flames, Combust. Flame 145 (2006) 401–414.
[34] R. W. Pitz, S. Hu, P. Wang, Tubular premixed and diffusion flames: Effect of stretch and curvature, Prog. Energy Combust. Sci. 42 (1) (2014) 1–34.
[35] I. Glassman, R. A. Yetter, N. G. Glumac, Combustion, 5th ed., Elsevier, 2015.
[36] A. C. Eckbreth, Laser diagnostics for combustion temperature and species, 2nd ed., Taylor & Francis, New York, NY, 1996, 400.
[37] J. B. Schmidt, S. Roy, W. D. Kulatilaka, I. Shkurenkov, I. V Adamovich, W. R. Lempert, J. R. Gord, Femtosecond, two-photon-absorption, laser-induced-fluorescence (fs-TALIF) imaging of atomic hydrogen and oxygen in non-equilibrium plasmas, J. Phys. D. Appl. Phys. 50 (1) (2017) 1–17.
[38] W. D. Kulatilaka, N. Jiam, S. Roy, J. R. Gord, High-repetition-rate imaging of atomic oxygen in flames, in 8th U.S. National Combustion Meeting, 070DI-0146, Salt Lake City, Utah, 2013.
[39] D. J. Bamford, L. E. Jusinski, W. K. Bischel, Absolute two-photon absorption and three-photon ionization cross sections for atomic oxygen, Phys. Rev. A 34 (1) (1986) 185–198.

[40] J. Bittner, K. Kohse-Höinghaus, U. Meier, T. Just, Quenching of two-photon-excited H(3s, 3d) and O(3p $^3P_{2,1,0}$) atoms by rare gases and small molecules, Chem. Phys. Lett. 143 (6) (1988) 571–576.
[41] J. Kojima, Q.-V. Nguyen, Laser pulse-stretching with multiple optical ring cavities, Appl. Opt. 41 (30) (2002) 6360–6370.
[42] C. A. Hall, Instability of premixed lean hydrogen laminar tubular flames, PhD Dissertation, Vanderbilt University, 2016.
[43] A. E. Lutz, R. J. Kee, J. F. Grcar, F. M. Rupley, OPPDIF: A fortran program for computing opposed-flow diffusion flames, in SAND96-8243, 1997.
[44] H. Schlichting, Boundary Layer Theory, 7th ed., McGraw-Hill, 1979, 95–99.
[45] M. D. Smooke, V. Giovangigli, Extinction of tubular premixed laminar flames with complex chemistry, Proc. Combust. Inst. 23 (1990) 447–454.
[46] R. S. Barlow, A. N. Karpetis, J. H. Frank, J. Y. Chen, Scalar profiles and NO formation in laminar opposed-flow partially premixed methane/air flames, Combust. Flame 127 (3) (2001) 2102–2118.
[47] R. J. Kee, F. M. Rupley, E. Meeks, J. A. Miller, Chemkin-II: A fortran chemical kinetics package for the analysis of gas-phase chemical and plasma kinetics, Report No. SAND-89-8009, Sandia National Laboratories, 1989.
[48] A. Ern, V. Giovangigli, Fast and accurate multicomponent transport property evaluation, J. Comput. Phys. 120 (1) (1995) 105–116.
[49] S. Balay, W. D. Gropp, L. C. McInnes, B. F. Smith, Efficient management of parallelism in object oriented numerical software libraries, in *Modern Software Tools in Scientific Computing*, E. Arge, A. Bruaset, and H. Langtangen, Eds. Birkhäuser Press, 1997, pp.163–202.
[50] G. J. Marshall, P. S. Walsh, R. W. Pitz, Quantitative oxygen atom measurements in lean, premixed, H_2 tubular flames, Proc. Combust. Inst. 38 (2020) in press. doi.org/10.1016/j.proci.2020.08.043
[51] M. P. Burke, M. Chaos, Y. Ju, F. L. Dryer, S. J. Klippenstein, Comprehensive H_2/O_2 kinetic model for high-pressure combustion, Int. J. Chem. Kinet. 44 (7) (2012) 444–474.
[52] J. Li, Z. Zhao, A. Kazakov, M. Chaos, F. L. Dryer, J. J. Scire, A comprehensive kinetic mechanism for CO, CH_2O, and CH_3OH combustion, Int. J. Chem. Kinet. 39 (2) (2007) 109–136.
[53] A. Kéromnès, W. K. Metcalfe, K. A. Heufer, N. Donohoe, A. K. Das, C.-J. Sung, J. Herzler, C. Naumann, P. Griebel, O. Mathieu, M. C. Krejci, E. L. Petersen, W. J. Pitz, H. J. Curran, An experimental and detailed chemical kinetic modeling study of hydrogen and syngas mixture oxidation at elevated pressures, Combust. Flame 160 (6) (2013) 995–1011.
[54] T. Varga, C. Olm, T. Nagy, I. G. Zsély, É. Valkó, R. Pálvölgyi, H. J. Curran, T. Turányi, Development of a joint hydrogen and syngas combustion mechanism based on an optimization approach, Int. J. Chem. Kinet. 48 (8) (2016) 407–422.
[55] A. F. Ghoniem, Z. Zhao, G. Dimitrakopoulos, Gas oxy combustion and conversion technologies for low carbon energy: Fundamentals, modeling and reactors, Proc. Combust. Inst. 37 (1) (2019) 33–56.
[56] F. Liu, H. Guo, G. J. Smallwood, The chemical effect of CO_2 replacement of N_2 in air on the burning velocity of CH_4 and H_2 premixed flames, Combust. Flame 133 (4) (2003) 495–497.
[57] K. Niemi, V. Schulz-von der Gathen, H. F. Döbele, Absolute calibration of atomic density

measurements by laser-induced fluorescence spectroscopy with two-photon excitation, J. Phys. D. Appl. Phys. 34 (15) (2001) 2330–2335.
[58] W. D. Kulatilaka, J. H. Frank, T. B. Settersten, Interference-free two-photon LIF imaging of atomic hydrogen in flames using picosecond excitation, Proc. Combust. Inst. 32 (1) (2009) 955–962.
[59] L. Gasnot, P. Desgroux, J. F. Pauwels, L. R. Sochet, Improvement of two-photon laser induced fluorescence measurements of H- and O-atoms in premixed methane/air flames, Appl. Phys. B 65 (4–5) (1997) 639–646.
[60] J. H. Frank, T. B. Settersten, Two-photon LIF imaging of atomic oxygen in flames with picosecond excitation, Proc. Combust. Inst. 30 (1) (2005) 1527–1534.
[61] P. Wang, X. Luo, Q. Li, Heat transfer study of the Hencken burner flame, Flow, Turbul. Combust. 101 (3) (2018) 795–819.
[62] D. Goodwin, H. Moffat, R. Speth, Cantera: An object-oriented software toolkit for chemical kinetics, thermodynamics, and transport properties, 2009. [Online]. Available: http://www.cantera.org.
[63] C. A. Hall, R. W. Pitz, A structural study of premixed hydrogen-air cellular tubular flames, Proc. Combust. Inst. 34 (1) (2013) 973–980.
[64] C. D. Carpenter, R. W. Pitz, Filtered Rayleigh scattering measurements of temperature in cellular tubular flames, Exp. Fluids 61 (45) (2020).
[65] W. D. Kulatilaka, B. D. Patterson, J. H. Frank, T. B. Settersten, Comparison of nanosecond and picosecond excitation for interference-free two-photon laser-induced fluorescence detection of atomic hydrogen in flames, Appl. Opt. 47 (26) (2008) 4672–4683.
[66] C. A. Hall, R. W. Pitz, Experimental and numerical study of H_2-air non-premixed cellular tubular flames, Proc. Combust. Inst. 36 (2016) 1595–1602.
[67] D. C. Tinker, C. A. Hall, R. W. Pitz, Partially premixed hydrogen-air cellular flames in a tubular burner, in 54th AIAA Aerospace Sciences Meeting AIAA 2016-1204, San Diego, CA, 2016.
[68] I. A. Mulla, A. Dowlut, T. Hussain, Z. M. Nikolaou, S. R. Chakravarthy, N. Swaminathan, R. Balachandran, Heat release rate estimation in laminar premixed flames using Laser-Induced Fluorescence of CH_2O and H-Atom, Combust. Flame 165 (2016) 373–383.
[69] M. B. Long, P. S. Levin, D. C. Fourguette, Simultaneous two-dimensional mapping of species concentration and temperature in turbulent flames, Opt. Lett. 10 (6) (1985) 267–269.
[70] D. C. Tinker, C. A. Hall, R. W. Pitz, Measurement and simulation of partially-premixed cellular tubular flames, Proc. Combust. Inst. 37 (2) (2019) 2021–2028.
[71] D. C. Tinker, C. A. Hall, R. W. Pitz, Major species measurements and simulation of partially-premixed, cellular, tubular H_2-air flames, in 55th AIAA Aerospace Sciences Meeting AIAA 2017-1801, Grapevine, TX, 2017.
[72] S. J. Kline, F. A. McClintock, Describing undertainties in single-sample experiments, Mech. Eng. 75 (1953) 3–8.
[73] S. Hu, P. Wang, R. W. Pitz, M. D. Smooke, Experimental and numerical investigation of non-premixed tubular flames, Proc. Combust. Inst. 31 (2007) 1093–1099.
[74] J. F. Grcar, The twopnt program for boundary value problems, in SAND91-8230, 1991.

A. Uncertainty Analysis

Number density uncertainty for the atomic oxygen measurements is considered to be a function of shot-to-shot signal fluctuation and the uncertainty associated with volumetric quenching rate measurements, k [40], as well as Raman measurements ($\pm$2% mole fraction, $\pm$70 K at flame temperatures, and $\pm$3 K at ambient)[14, 42, 63]. The value of uncertainty from determining C is expected to be insignificant compared to the other sources of deviation (see calibration curve of 4.2.3 Calibration Methods [50]). Equation 2.4 is restated below for quick reference as Equation A.1 stems directly from it.

$$N_O = C\frac{A+Q}{A}S \tag{2.4}$$

The following method employs the Kline-McClintock approach of determining uncertainties [72]. Signal deviation due to changes in laser fluence during imaging was approximated as $\pm$2% by the sample standard deviation of the 10 frames (10,000 total laser pulses) captured at each location. The following equation may be used to estimate atomic oxygen concentration uncertainty by combining the signal, sig, fluctuation with uncertainty in volumetric quenching rate, k, major species concentration, and temperature:

$$u_{N_O} = \frac{U_A}{A} + \frac{U_A + U_Q}{A+Q} + u_{sig} \tag{A.1}$$

where u and U refer to relative and absolute uncertainties, respectively. Subscripts represent the value being quantified. A mix of relative and absolute uncertainties is given in Eq. A.1 based on the type of values provided in literature and the most convenient method to calculate the quenching uncertainty, U_Q, namely:

$$U_Q = \sum_i \left(\frac{U_{k_i}}{k_i} + u_{Ram_i} + \frac{U_T}{T}\right) k_i X_i \frac{P}{k_b T} \tag{A.2}$$

where the subscript Ram_i refers to Raman-collected data for the i^{th} species, P is atmospheric pressure, and k_b is the Boltzmann constant. The $\frac{P}{k_b T}$ term is necessary to convert mole fraction to number densities for each quenching species.

Uncertainty was evaluated at each location in the flames from the above equations and varied slightly across the radius. This change occurs as temperature increases across the flame zone while applying the absolute uncertainty values. Fluctuations are lower in the reactant zone where temperature is more precisely known. Relative number density uncertainties were found to be $\pm$16, 27, and 18% for N_2-diluted flames in the reactant, flame, and product zones and $\pm$8, 20, and 12% in the reactant, flame, and product zones of the data for CO_2-diluted flames. Reduced uncertainty in the CO_2 compared to N_2-diluted data arises from decreased uncertainty in its measured k value [40].

B. TUBEDIF

The following is a brief discussion of the non-cellular (1D) solver used to model the flames of Chapter 4. The commercial, CHEMKIN-based code OPPDIF [43] was previously modified by Chih-Jen Sung [13] and Mitchell Smooke [73] for premixed and non-premixed flames respectively. Their work was combined into one code, TUBEDIF.

Please reference NOMENCLATURE and Chapter 3 for variable explanations. The radial and axial components of the velocity field are represented by F and G, respectively, while the pressure eigenvalue is again give as H:

$$F = -\rho r u \tag{B.1}$$

$$G = \rho r W \tag{B.2}$$

$$H = \frac{1}{z}\frac{\partial \tilde{p}_1}{\partial z} \tag{B.3}$$

The steady-state conservation equations are expressed in terms of the above variables along with mass fraction (Y_i) and temperature (T) to arrive at the following:

Mass conservation,

$$0 = G - \frac{\mathrm{d}F}{\mathrm{d}r} \tag{B.4}$$

Axial momentum conservation,

$$0 = -\rho r F \frac{\mathrm{d}}{\mathrm{d}r}\left(\frac{G}{\rho r}\right) - \rho r \frac{\mathrm{d}}{\mathrm{d}r}\left[\mu r \frac{\mathrm{d}}{\mathrm{d}r}\left(\frac{G}{\rho r}\right)\right] + \rho r^2 H + G^2 \tag{B.5}$$

Eigenvalue equation,

$$0 = \frac{\mathrm{d}H}{\mathrm{d}r} \tag{B.6}$$

Energy conservation,

$$0 = -\frac{F}{r}\frac{\mathrm{d}T}{\mathrm{d}r} - \frac{1}{rc_p}\frac{\mathrm{d}}{\mathrm{d}r}\left(\lambda r\frac{\mathrm{d}T}{\mathrm{d}r}\right) + \frac{1}{c_p}\sum_{i\epsilon\mathcal{S}}\left(\rho Y_i u_i^d c_{p_i}\frac{\mathrm{d}T}{\mathrm{d}r}\right) + \frac{1}{c_p}\sum_{i\epsilon\mathcal{S}}\left(\omega_{s_i}h_i\right) + \frac{1}{c_p}Q_{rad} - \frac{1}{rc_p}\frac{\mathrm{d}}{\mathrm{d}r}(rq^D) \tag{B.7}$$

Chemical species conservation,

$$0 = -\frac{F}{r}\frac{\mathrm{d}Y_i}{\mathrm{d}r} + \frac{1}{r}\frac{\mathrm{d}}{\mathrm{d}r}\left(r\rho Y_i u_i^d\right) - \omega_{s_i}W_i, \qquad i\,\epsilon\,\mathcal{S} \tag{B.8}$$

The radial diffusion velocity of species i, u_i^d is related to

$$\rho Y_i u_i^d = \sum_{j\epsilon\mathcal{S}}\left(Y_i\mathcal{D}_{ij}\frac{\mathrm{d}x_j}{\mathrm{d}r}\right) - Y_i\mathcal{D}_i^T\frac{1}{T}\frac{\mathrm{d}T}{\mathrm{d}r}, \qquad i\,\epsilon\,\mathcal{S} \tag{B.9}$$

The domain is defined over $r\,\epsilon\,[0, R_0]$ where R_0 is the outer radius of the burner nozzle, 12 mm. The boundary conditions for the premixed configuration at $r = 0$ are set to the following:

$$F = 0, \qquad \frac{\mathrm{d}}{\mathrm{d}r}T = 0, \qquad \frac{\mathrm{d}}{\mathrm{d}r}G = 0, \qquad \frac{\mathrm{d}}{\mathrm{d}r}Y_k = 0, k\,\epsilon\,\mathcal{S}$$

for $r = R_0$

$$F = -(\rho Ru)_{BC}, \qquad T = T_{BC}, \qquad G = (\rho RW)_{BC}, \qquad \rho Y_k\left(u + u_k^d\right) = (\rho Y_k u)_{BC}, k\,\epsilon\,\mathcal{S}$$

TWOPNT [74] is used to implicitly solve the governing equations on a radially adaptive grid to better resolve variables in high-gradient regions.